The Astrophysical Journal, 973:125 (18pp), 2024 October 1 https://doi.org/10.3847/1538-4357/ad6004

Discovery of a Metal-poor Red Giant Star with the Highest Ultralithium Enhancement

Jeremy Kowkabany[1,2], Rana Ezzeddine[1,3], Corinne Charbonnel[4,5], Ian U. Roederer[3,6], Ella Xi Wang[7,8], Yangyang Li[1], Zoe Hackshaw[9], Timothy C. Beers[3,10], Anna Frebel[3,11], Terese T. Hansen[12], Erika Holmbeck[3,13], Vinicius M. Placco[14], and Charli M. Sakari[15]

[1] Department of Astronomy, University of Florida, Gainesville, FL 32601, USA; rezzeddine@ufl.edu
[2] Department of Physics, Florida State University, Tallahassee, FL 32306, USA
[3] Joint Institute for Nuclear Astrophysics—Center for Evolution of the Elements, USA
[4] Department of Astronomy, University of Geneva, Chemin de Pégase 51, 1290 Versoix, Switzerland
[5] IRAP, CNRS UMR 5277 and Université de Toulouse, 14 av. E. Belin, 31400 Toulouse, France
[6] Department of Physics, North Carolina State University, Raleigh, NC 27695, USA
[7] Research School of Astronomy and Astrophysics, Australian National University, Canberra, ACT 2611, Australia
[8] ARC Centre of Excellence for All Sky Astrophysics in 3 Dimensions (ASTRO 3D), Canberra, ACT 2611, Australia
[9] Department of Astronomy, University of Texas at Austin, 2515 Speedway, Austin, TX 78712-1205, USA
[10] Department of Physics and Astronomy, University of Notre Dame, Notre Dame, IN 46556, USA
[11] Department of Physics & Kavli Institute for Astrophysics and Space Research, Massachusetts Institute of Technology, Cambridge, MA 02139, USA
[12] Department of Astronomy, Stockholm University, AlbaNova University Centre, SE-106 91 Stockholm, Sweden
[13] Lawrence Livermore National Laboratory, 7000 East Avenue, Livermore, CA 94550, USA
[14] NSF's NOIRLab, 950 N. Cherry Avenue, Tucson, AZ 85719, USA
[15] San Francisco State University, 1600 Holloway Avenue, San Francisco, CA 94132, USA

Received 2022 August 23; revised 2024 July 1; accepted 2024 July 1; published 2024 September 26

Abstract

We present the discovery of 2MASS J05241392−0336543 (hereafter J0524−0336), a very metal-poor ([Fe/H] = −2.43 ± 0.16), highly r-process-enhanced ([Eu/Fe] = +1.34 ± 0.10) Milky Way halo field red giant star, with an ultrahigh Li abundance of A(Li, 3D, NLTE) = 6.15 ± 0.25 and [Li/Fe] = +7.64 ± 0.25, respectively. This makes J0524−0336 the most lithium-enhanced giant star discovered to date. We present a detailed analysis of the star's atmospheric stellar parameters and chemical abundance determinations. Additionally, we detect indications of infrared excess, as well as observe variable emission in the wings of the Hα absorption line across multiple epochs, indicative of a potential enhanced mass-loss event with possible outflows. Our analysis reveals that J0524−0336 lies either between the bump and the tip of the red giant branch (RGB), or on the early asymptotic giant branch (e-AGB). We investigate the possible sources of lithium enrichment in J0524−0336, including both internal and external sources. Based on current models and on the observational evidence we have collected, our study shows that J0524−0336 may be undergoing the so-called lithium flash that is expected to occur in low-mass stars when they reach the RGB bump and/or the e-AGB.

Unified Astronomy Thesaurus concepts: Chemical abundances (224); R-process (1324); Lithium stars (927); Asymptotic giant branch (108); Red giant bump (1369); Milky Way stellar halo (1060)

Materials only available in the online version of record: machine-readable table

1. Introduction

Observational evidence has accumulated on the decrease of the lithium (Li) photospheric abundance in low-mass stars as they age. Li depletion is observed to occur already on the pre–main sequence for very low-mass stars, and along the main sequence with mass and age-dependent efficiency that cannot be explained by so-called classical stellar-evolution models (e.g., Charbonneau & Michaud 1990; Soderblom et al. 1993; Lyubimkov 2016; Tognelli et al. 2021; Binks et al. 2022). The observed Li patterns instead reveal the occurrence of internal transport processes of chemical elements other than convection in low-mass stars. (e.g., Deliyannis et al. 2000; Talon & Charbonnel 2010). Models including atomic diffusion and turbulence are almost fully bridging the gap between the primordial (Big Bang nucleosynthesis) Li abundance and the Li observed in metal-poor warm turnoff stars along the Spite plateau and in globular clusters (e.g., Richard et al. 2005; Korn et al. 2006; Nordlander et al. 2012; Gruyters et al. 2016; Gao et al. 2020; Deal & Martins 2021). Also, the Li depletion in more metal-rich stars like the Sun and F- and G-type dwarfs in open clusters can be self-consistently reproduced when accounting for different hydrodynamical processes that transport both matter and angular momentum in stellar interiors (e.g., Charbonnel & Talon 2005; Dumont et al. 2021a, 2021b, and references therein).

The photospheric Li keeps decreasing during the so-called first dredge-up when low-mass stars evolve toward the red giant branch (RGB; e.g., Iben 1967), as evidenced both in metal-poor stars from the halo and globular clusters and in metal-rich stars in the field and in open clusters (e.g., Lèbre et al. 1999; Charbonnel et al. 2000, 2020; Lind et al. 2009; Canto Martins et al. 2011; Magrini et al. 2021a; Aguilera-Gómez et al. 2022; Mucciarelli et al. 2022). Later, Li decreases again sharply as soon as the stars reach the luminosity of the bump on the upper RGB (e.g., Charbonnel et al. 1998, 2020; Gratton et al. 2000; Lind et al. 2009). This last Li depletion episode has been suggested to be attributed to thermohaline mixing, which is a double diffusive process that has been suggested to connect the base of the convective envelope to the hydrogen-burning shell of low-mass red giants and expected to decrease their photospheric Li abundance and carbon isotopic ratio simultaneously (Charbonnel & Zahn 2007; Charbonnel & Lagarde 2010). Angelou et al. (2015) showed that their models, however, predicted that the mixing would start at a higher luminosity than predicted by that data, and that it was not possible to simultaneously reproduce the evolution of carbon and lithium abundance on the RGB. Given the universality of the first dredge-up in low-mass stellar evolution, and the sensitivity of lithium to mixing processes as evidenced for both metal-poor and metal-rich dwarf and giant stars, one could reasonably expect to observe low lithium abundances in all low-mass giant stars, independently of their initial metal content. While this is generally the case, a small fraction of low-mass red giants exhibit exceptionally high Li abundances.

The enhancement of lithium in red giant stars is a rare and continuously not understood phenomenon since its discovery by Wallerstein & Sneden (1982). As lithium is easy to observe in cool stars, many spectroscopic surveys have looked for Li-rich stars (Brown et al. 1989; Jasniewicz et al. 1999; Charbonnel & Balachandran 2000; Monaco et al. 2011; Lyubimkov et al. 2012; Martell & Shetrone 2013; Liu et al. 2014; Bharat Kumar et al. 2015; De Silva et al. 2015; Smiljanic et al. 2018; Zhou et al. 2018; Gao et al. 2019; Charbonnel et al. 2020; Deepak et al. 2020; Magrini et al. 2021b; Martell et al. 2021). Depending on the adopted criteria for a star to be classified as Li rich (see the discussions in Charbonnel et al. 2020; Chanamé et al. 2022), all surveys show that roughly 1% of red giant stars have enhanced photospheric lithium abundances with respect to their Li-depleted counterparts. Of the lithium-rich giants discovered in the last three decades (e.g., Casey et al. 2019; Gao et al. 2019; Martell et al. 2021; Cai et al. 2023), only about 3% have been observed to be superLi rich, with an abundance of $A(\mathrm{Li})$[16] > 3.3 dex, i.e., higher than the protosolar Li abundance. Accounting for non–local thermodynamic equilibrium (NLTE) for Li abundances, only a handful of stars have been found to have an abundance of $A(\mathrm{Li}) > 4$ (Balachandran et al. 2000; Martell & Shetrone 2013; Strassmeier et al. 2015; Casey et al. 2016; Yan et al. 2018; Singh et al. 2019; Susmitha et al. 2024).

Two general ideas have been explored to account for the excess amounts of lithium present in this minority of stars, namely, the production of fresh Li inside the stars themselves, or the accretion of Li-rich material from an external source. Internal Li production in red giants requires a fast transport process in the radiative layers between the hydrogen-burning shell where unstable ^{7}Be can be produced through *pp* chains and the base of the convective envelope where Li can survive[17] (Sackmann & Boothroyd 1999; Charbonnel & Balachandran 2000; Denissenkov & Weiss 2000; Palacios et al. 2001; Denissenkov & Herwig 2004; Silva Aguirre et al. 2014; Yan et al. 2018; Casey et al. 2019; Mori et al. 2021). A number of plausible external mechanisms have also been suggested, including planetary engulfment or nova debris contaminating the outer layers of these giants (Alexander 1967; Andrievsky et al. 1999; Siess & Livio 1999; Aguilera-Gómez et al. 2016; Casey et al. 2016; Mallick et al. 2022). The occurrence and the efficiency of these different mechanisms are expected to depend on the evolution stage of the Li-rich stars. Recently, Yan et al. (2021), Deepak & Lambert (2021), and Chanamé et al. (2022) showed using asteroseismology that the majority of the Li-rich giant stars are in their core helium-burning phase (red clump (RC)), while a smaller fraction of Li-rich stars have been found to be high on the RGB (red bump), including the extremely high Li-rich star TYC 429-2097-1 (Yan et al. 2018). It is thus yet to be established whether Li enrichment is strictly attributed to one or more evolutionary status of stars; such a connection can only be evidenced by the influx of more asteroseismic data for newly discovered Li-rich stars.

Table 1
Properties of J0524−0336

Label	Value
Two Micron All-Sky Survey (2MASS) star ID	2MASS J05241392−0336543
Gaia Data Release 3 (DR3) ID	3210839729979320064
R.A. (J2000)	05:24:13.900
Decl. (J2000)	−03:37:00.300
$G_{\rm mag}$ (Gaia DR3)	13.343
$V_{\rm mag}$ (Gaia DR3)[a]	13.904
$V_{\rm mag}$ (Large Sky Area Multi-Object Fibre Spectroscopic Telescope (LAMOST))	13.894
$v_{\rm rad}^{\rm helio}$(this work, units of km s^{-1})	103.10 ± 0.80
$v_{\rm rad}^{\rm helio}$(Gaia DR3, units of km s^{-1})	102.79 ± 1.35
$T_{\rm eff}$ (K)	4540 ± 150
$\log g$	1.09 ± 0.26
ξ_t (km s^{-1})	2.37 ± 0.08
[Fe/H]	-2.54 ± 0.17
$v_{\sin i}$ (km s^{-1})	11 ± 2
$\log(L/L_\odot)$	2.57 ± 0.11
R ($R_\odot$)	32 ± 5

Note.
[a] V magnitude determined from the Gaia DR3 G magnitudes and $BP - RP$ color conversions.

It is within this context that we present our discovery of a unique ultraenhanced lithium giant metal-poor Milky Way (MW) halo star, 2MASS J05241392−0336543 (hereafter referred to as J0524−0336), discovered serendipitously as part of the *R*-Process Alliance (RPA) survey. Initial high-resolution spectroscopic data collected for this star suggested a lithium abundance far greater than the Li-rich standard of $A(\mathrm{Li}) \sim 1.5$. We then further collected higher signal-to-noise-ratio (S/N) high-resolution data for the star to confirm this enhancement, and several epochs of observations to monitor its radial velocity (RV). The fundamental properties of J0524−0336 are listed in Table 1, with detailed description explained in the sections to follow.

This paper is outlined as follows: In Section 2, we describe our observations, data reduction, and RV determinations for the candidate star. In Section 3, we thoroughly investigate the fundamental atmospheric stellar parameters, using different methods including 1D LTE as well as NLTE radiative transfer analyses, and use photometric measurements to establish the stellar evolutionary status of J0524−0336. In Section 4, we present the detailed chemical abundance determinations in our star, including abundances of the light, α, and *r*-process elements, as well as comparison with previously discovered lithium-rich giants. In Section 5, we discuss the evolutionary status of J0524−0336 based on tailor-made stellar-evolution

---

[16] $A(\mathrm{Li}) = \log_{10}(N_{\rm Li}/N_{\rm H}) + 12$.

[17] This is the so-called Cameron & Fowler (1971) process, which is expected to occur in the convective envelope of Li-rich stars on the asymptotic giant branch (AGB; Sackmann & Boothroyd 1992; Forestini & Charbonnel 1997).

models. Finally, we present our discussion of the results and conclusions in Sections 6 and 7, respectively.

2. Observations and Data Reduction

J0524−0336 was initially identified and vetted as an *r*-process-enhanced candidate by the RPA collaboration (Hansen et al. 2018; Sakari et al. 2018; Ezzeddine et al. 2020; Holmbeck et al. 2020), from the LAMOST survey (Deng et al. 2012). The star was observed with the Magellan Inamori Kyocera Echelle (MIKE) spectrograph (Bernstein et al. 2003) on the Magellan-Clay Telescope at Las Campanas Observatory on three separate nights: for 1200 s on 2018 March 8, for 7600 s, on 2019 October 26, as well as for 120 s on 2022 March 3. All observations were taken with the 0.″7 slit with the 2×2 binning setup, yielding nominal resolving powers of $R \sim 35{,}000$ in the red ($\lambda > 5000$ Å) and $R \sim 41{,}000$ in the blue.

The spectra were then reduced using the latest versions of the `Carnegie Python distribution`[18] (Kelson 2003). Each order of each spectrum was afterwards normalized and merged into a final spectrum, covering a wavelength range of ∼3320–9165 Å. For our final analysis of J0524−0336, we use the highest-S/N spectrum from 2019 October, with S/N ∼ 25 (pixel^{-1}) at 3950 Å, ∼70 at 4550 Å, ∼85 at 5200 Å, and ∼240 at 6750 Å. The final spectrum was RV, $v_{\rm rad}$, shifted by cross correlation with the Mg I lines near 5100 Å from the spectrum of the benchmark metal-poor star HD 122563, using the spectroscopic analysis tool `Spectroscopy Made Hard` (SMH; Casey 2014). A heliocentric velocity ($v_{\rm rad}^{\rm helio}$) correction was then determined with the `rvcorrect` package in `IRAF` (Tody 1986), with $v_{\rm rad}^{\rm helio} = 103.10 \pm 0.90$ km s^{-1}. This value is in good agreement with the Gaia DR3 heliocentric RV $v_{\rm rad}^{\rm Gaia} = 102.79 \pm 1.35$ km s^{-1}. We also determine $v_{\rm rad}^{\rm helio} = 102.10 \pm 1.00$ km s^{-1} from the 2022 data and $v_{\rm rad}^{\rm helio} = 101.40 \pm 0.90$ km s^{-1} from the 2018 data. Based on the present data there is no evidence to support that J0524−0336 is in a binary system.

3. Stellar Properties and Fundamental Atmospheric Parameters

Due to the significant Li enhancement of our star ((Li, 3D, NLTE) $= 6.15 \pm 0.20$; see Section 4), we conduct a thorough investigation of its stellar parameters, in an attempt to accurately identify its stellar evolutionary status. We thus investigate the fundamental atmospheric stellar parameters (namely, the effective temperature $T_{\rm eff}$, surface gravity $\log g$, metallicity [Fe/H], and microturbulent velocity ξ_t) of J0524−0336 using spectroscopic LTE and NLTE radiative transfer models, as well as with nonspectroscopic methods implementing photometry and fundamental equations. Additionally, we investigate its stellar properties relevant to the current study, including its luminosity, radius, projected rotational velocity $v_{\sin i}$, infrared (IR) excess, and Hα emission. Below, we describe the methods and report on each of our derived properties and parameters separately.

3.1. Local Thermodynamic Equilibrium Stellar Parameters

We determine the fundamental atmospheric stellar parameters of J0524−0336 under the assumption of LTE using abundances of 178 Fe I and 17 Fe II lines, and employing the 2017 version of the LTE radiative transfer code `MOOG` (Sneden 1973), which includes a Rayleigh scattering treatment following Sobeck et al. (2011).[19] The Fe I and Fe II line list was adopted from Roederer et al. (2018), with $\log gf$ values compiled from several sources (see their Table 2 and references therein). Abundances were computed using 1D LTE, α-enhanced stellar atmospheric models from Castelli & Kurucz (2004), including standard α-element enhancement of $[\alpha/{\rm Fe}] = +0.4$. The abundances of Fe I and Fe II were determined using the equivalent width (EW) curve-of-growth (COG) method. The EW measurements were done by fitting Gaussian line profiles to the absorption lines using `SMH`. $T_{\rm eff}$ was determined by establishing excitation equilibrium of the Fe I abundance lines as a function of excitation potential, χ. $\log g$ was determined by establishing an ionization equilibrium between the abundances derived from the Fe I and Fe II lines. ξ_t was estimated by requiring no trend between the abundances derived from the Fe I lines and the reduced EWs ($\log({\rm EW}/\lambda)$). [Fe/H] was determined from the average of the Fe I and Fe II line abundances. The derived LTE stellar parameters are $T_{\rm eff} = 4300 \pm 150$ K, $\log g = 0.02 \pm 0.3$, $\xi_t = 3.14 \pm 0.2$ km s^{-1}, and $[{\rm Fe/H}] = -2.57 \pm 0.14$. We estimate parameter uncertainties for $T_{\rm eff}$, $\log g$, and ξ_t assuming systematic uncertainties following the analysis in Ji et al. (2016). The [Fe/H] uncertainties were determined from the standard deviations of the Fe I and Fe II abundances.

3.2. Non–Local Thermodynamic Equilibrium Stellar Parameters

Atmospheric stellar-parameter determinations for metal-poor stars from LTE spectroscopic methods are affected by unaccounted-for departures from statistical equilibrium that can introduce significant systematic uncertainties, since line formation and the populations of nondominant species (in this case Fe I) can potentially deviate from the Saha–Boltzmann equilibrium assumed in LTE (Lind et al. 2012; Amarsi et al. 2016; Ezzeddine et al. 2017). To account for such departures, it is necessary to investigate the formation of iron lines (and thus stellar parameters) in NLTE.

Therefore, we also determine stellar parameters for J0524−0336 using 1D NLTE radiative transfer models. The NLTE abundances were computed for the Fe I and Fe II lines from their EWs using the radiative transfer code `MULTI` in its 2.3 version (Carlsson 1986, 1992), and employing 1D `MARCS` model atmospheres (Gustafsson et al. 1975, 2008) interpolated to the corresponding parameters. Blanketing from background opacities, excluding Fe lines, was employed from the `MARCS` opacity package (B. Plez 2024, private communication).

The Fe I/Fe II atomic model used in the NLTE calculations is described in Ezzeddine et al. (2016, 2017). This model was built by adopting up-to-date atomic data, taking into account inelastic collisions with neutral hydrogen rates for excitation and charge-exchange processes as implemented from Barklem (2018). These collisions play an important dominant role (over electrons) in NLTE calculations of cool stars.

The NLTE stellar parameters were derived using the 1D NLTE atmospheric stellar parameters optimization tool `LOTUS`[20] (Li & Ezzeddine 2023). The tool utilizes the same optimization conditions described in Section 3.1 to derive the

---

[18] https://code.obs.carnegiescience.edu/mike

[19] https://github.com/alexji/moog17scat

[20] https://github.com/Li-Yangyang/LOTUS

Table 2
Stellar Atmospheric Parameters of J0524−0336

Parameter	LTE	NLTE	Adopted
$T_{\rm eff}$ (K)	4300 ± 150	4540 ± 150	4540 ± 150
$\log g$	0.02 ± 0.30	1.09 ± 0.26	1.09 ± 0.26
ξ_t (km s^{-1})	3.14 ± 0.20	2.37 ± 0.08	2.37 ± 0.08
[Fe/H]	−2.57 ± 0.14	−2.54 ± 0.17	−2.54 ± 0.17

parameters (i.e., excitation and ionization equilibrium), and employs a global COG method to take into account the interdependence of the EW of each Fe I and Fe II line on the corresponding atmospheric stellar parameters. Additionally, error bars were constrained using a Markov Chain Monte Carlo algorithm. The NLTE parameters are $T_{\rm eff} = 4540 \pm 150$ K, $\log g = 1.09 \pm 0.26$, $[{\rm Fe/H}] = -2.54 \pm 0.17$, and $\xi_t = 2.37 \pm 0.08$ km s^{-1}.

3.3. Fundamental Stellar Parameters

We derive a luminosity of $L = 371 \pm 90$ $L_\odot$, with $\log(L/L_\odot) = 2.57 \pm 0.11$. The luminosity was calculated using the fundamental equations,

$$-2.5\log\left(\frac{L}{L_\odot}\right) = M_V - M_{V,\odot}, \quad (1)$$

$$M_V = m_V + 5 - 5\log d - A_V, \quad (2)$$

where M_V and m_V are the absolute and apparent magnitudes, respectively, $M_{V,\odot} = 4.83$ the solar absolute magnitude, d the distance from Gaia DR3, and $A_V \approx R_V * E(B - V)$ is the extinction. The apparent visual magnitude ($m_V = 13.894$) is from LAMOST (compares well to the $m_V = 13.904$ which was derived the from Gaia EDR3 $m_G = 13.348$), and the distance, $d = 9065.45 \pm 1228.1$ pc, was adopted from Bailer-Jones et al. (2021) derived from the Gaia EDR3 parallax. The extinction value, $E(B - V) = 0.229$, is from Schlafly & Finkbeiner (2011). With the luminosity determined, the radius $R = 32 \pm 5$ $R_\odot$ is then derived using the equation,

$$R = \sqrt{\frac{L}{4\pi\sigma T^4}}, \quad (3)$$

assuming a blackbody and utilizing the NLTE temperature. We adopt mass $M = 0.8$ $M_\odot$, typical of evolved giant stars at the metallicity of our star.

Interestingly, J0524−0336 was also recently flagged as a variable star in Gaia DR3, with a G-magnitude variability difference between `max_mag_g_fov` and `min_mag_g_fov` of 0.153, with a median G magnitude of 13.343, and a period of 59.9 days. We note that J0524−0336 is also listed as variable in the ASAS-SN database (Shappee et al. 2014), with $V_{\rm max} - V_{\rm min} = 0.28$.

3.4. Adopted Atmospheric Fundamental Parameters

The derived fundamental atmospheric parameters of J0524−0336 using the different methods outlined in Sections 3.1–3.3 are listed in Table 2. The derived NLTE $T_{\rm eff}$ is ∼240 K higher than the LTE $T_{\rm eff}$, and the $\log g$ in NLTE is ∼1.0 dex higher than in LTE. Given that NLTE models are more realistic than LTE, we therefore adopt for our final parameters the NLTE values for J0524−0336, with $T_{\rm eff} = 4540 \pm 150$ K, $\log g = 1.09 \pm 0.26$, $\xi_t = 2.37 \pm 0.08$ km s^{-1}, and $[{\rm Fe/H}] = -2.54 \pm 0.17$. We will use these parameters throughout the rest of the paper.

3.5. Projected Rotational Velocity

Rotational velocity has been linked to both external and internal lithium enhancement (Carlberg et al. 2012; Charbonnel et al. 2020). A rapidly rotating star is defined as having a projected rotational velocity $v \sin i > 5$ km s^{-1} (Tayar et al. 2015). We determine the projected rotational velocity, $v_{\sin i}$, of J0524−0336 following two methods: (i) using the FWHMs of several Fe I lines around the 6400 Å region following the method outlined in Bruntt et al. (2010), as well as (ii) fitting the Fe I lines using synthetic spectra computed with different $v_{\sin i}$ values. We note that for both methods we fix the stellar parameters to those derived and adopted in Section 3.2.

We used six isolated iron lines ranging from 6400 to 6500 Å (S/N ∼ 240), and corrected their FWHMs for instrumental broadening using the correction values from Bruntt et al. (2010). The lines were chosen as they were strong, unblended, and had high S/Ns, following Bruntt et al. (2010). This yielded the intrinsic total broadening of the spectrum, which is contributed by both rotation and macroturbulence. In order to solve for the rotational velocity, we first estimated our star's macroturbulence ($v_{\rm macro} = 4.96 \pm 0.45$ km s^{-1}) using the equation for luminosity class III stars from Hekker & Meléndez (2007), and implementing the stellar parameters of our star. We determine $v_{\sin i} = 10.7 \pm 1.8$ km s^{-1}. We also independently fit synthetic line spectra computed with different $v_{\sin i}$ values to several Fe I lines in the 4000–6500 Å region of J0524−0336, as shown in Figure 1. To account for possible broadening sources, we take into account microturbulent velocity broadening, radiative (Doppler) and inelastic hydrogen collisional broadening (Van der Waals), as well as instrumental broadening based on the MIKE resolution (determined by convolving a Gaussian profile with each of the Fe I lines). Based on the fits, we estimate a projected rotational velocity, $v_{\sin i} \sim 11 \pm 2$ km s^{-1}, which is consistent with our FWHM calculations following Bruntt et al. (2010). This classifies J0524−0336 as a rapidly rotating red giant metal-poor star with a projected rotational velocity > 10 km s^{-1}.

3.6. Hα Emission and Infrared Excess

Lithium enhancement in stars has been suggested to be linked to stellar properties such as IR excess and Hα emission, as proposed in some studies such as Fekel & Watson (1998), Rebull et al. (2015), and Mallick et al. (2022). Both these properties, if observed in stars, are indicators of mass-loss events, which have been connected to multiple channels of lithium enhancement (de la Reza et al. 1996, 1997). We therefore investigate both IR excess and Hα emission in J0524−0336. Figure 2 shows the Hα line profile in J0524−0336, observed at three different epochs, in 2018, 2019, and 2022, respectively. Also shown, for comparison, is the Hα profile for the metal-poor star J0155−6400, with similar stellar parameters as J0524−0336 and no Li detection. We observe emission in the Hα wings in all observation epochs of J0524−0336. Interestingly, however, each of these emission profiles are different for each epoch, signifying strong and variable activity, possibly due to mass-loss events or the presence of a circumstellar disk around the star. Additionally, we note the

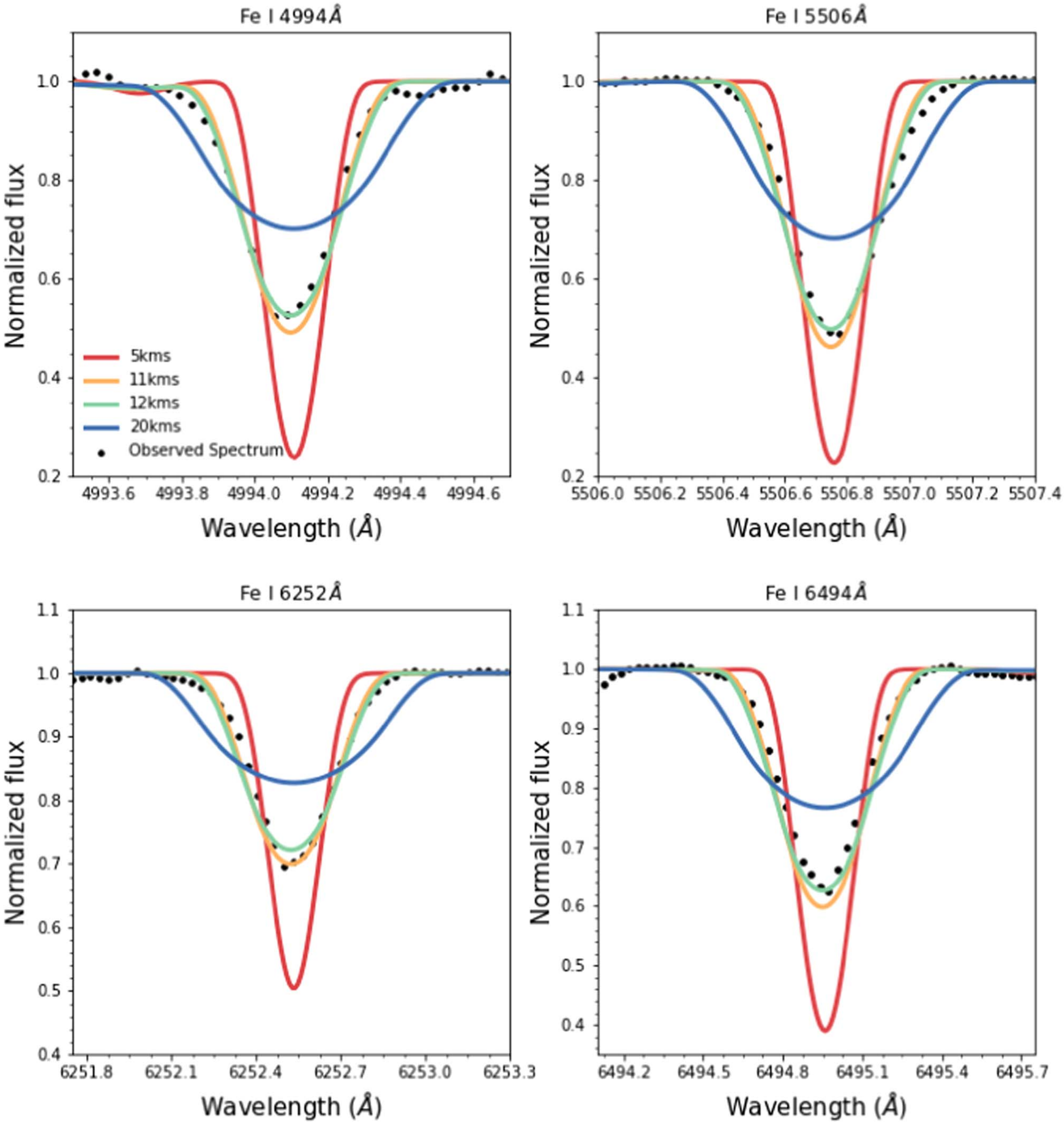

Figure 1. Synthetic spectral line profiles shown for four Fe I lines in J0524−0336, computed with different stellar projected rotational velocities $v \sin i$, ranging from 5 to 20 km s^{-1} (solid colored lines) shown against the observed spectra (dotted black points).

asymmetric nature of the emission around the wings, signifying possible outflows. Consequently, we also looked into the IR photometry for J0524−0336 from the Wide-field Infrared Survey Explorer (WISE)[21] all-sky data colors (Wright et al. 2010). The IR excess or enhancement in stars typically has a WISE band difference of $W1-W4>0.5$ (Yan et al. 2018; Martell et al. 2021). We note the WISE flags for our star: the contamination and confusion flag `cc_flags`, and the photometric quality flag `ph_qual` are set to `0000` and AAAC, respectively, implying a noncontaminated WISE detection with an S/N of 2–3. WISE reports $W1=10.402\pm0.023$ and $W4=8.773\pm0.362$ for J0524−0336, which yields $W1-W4=1.629$, indicating a possible strong IR excess, which further points to stellar activity and possible mass-loss events in J0524−0336. We warn though that the W4 magnitude reported in WISE has been flagged as being less certain than the W1 color, with a 4% error bar reported for W4 versus 0.2% for W1. We, therefore suggest that detailed spectral energy distribution fitting and more precise IR colors are needed to determine whether IR excess is confirmed in J0524−0336. Notably, IR excesses have been detected in 1% of all giant stars, as compared to the 7% lithium-enhanced giant stars discovered in the MW (Rebull et al. 2015; Martell et al. 2021). No clear connection has yet been made between IR excess and Li-rich

---

[21] https://wise2.ipac.caltech.edu/docs/release/allsky/

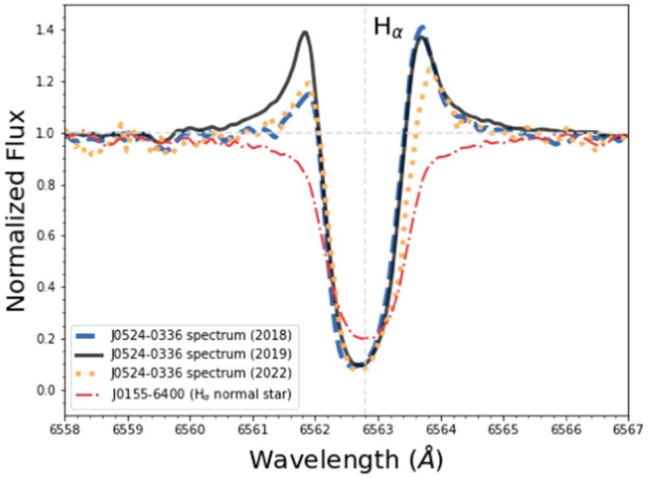

Figure 2. Hα line profile observed at different epochs in 2018, 2019, and 2022 in J0524−0336. Also shown, for comparison, is the Hα profile for the Hα-normal metal-poor star J0155−6400 with similar stellar parameters as J0524−0336.

stars, however, nontraditional mixing mechanisms enhancing photospheric Li abundances (such as rotation-driven mixing) might need to be invoked to explain this phenomenon.

4. Chemical Abundances

We derive abundance measurements, as well as upper limit estimates for the light, α, and Fe-peak elements for J0524−0336 using the same radiative transfer models and spectroscopic tools described in Section 3. We computed the abundance ratios relative to H and Fe, adopting the solar photospheric abundances from Asplund et al. (2009). The abundances were derived using a line-by-line EW and COG analysis, except for Li, C, O, Al, and the neutron-capture elements, where synthetic spectral profiles were fit to each line. The line list was adopted from Roederer et al. (2018, see their Table 2 for atomic data references) for lines which could be detected in J0524−0336. Isotopic ratios were included for Li, C (see below for details), as well as for several neutron-capture elements from Sneden et al. (2008)[22] and Placco et al. (2021). Hyperfine structure was considered for the Fe-peak elements, including Sc, V, Mn, and Co, when necessary. Upper limits were determined by matching the noise levels in the observed spectral lines with the corresponding synthetic spectral lines. Upon examining abundances from multiple lines for each element, outlying abundances (outside of 1σ) were removed and the average abundance and standard deviation were recorded for each element. For elements with only 2–5 lines measured, we estimated standard deviations by multiplying the range of values covered by our line abundances with the k-factor following Keeping (1962). For elements with one line only, we adopt an uncertainty between 0.1 and 0.3 dex, depending on the data and fit quality. The abundance averages and the corresponding standard deviations are reported in Table 3. The line-by-line abundances of each of these elements are recorded in Table 4. We record systematic uncertainties in our chemical abundances resulting from uncertainties in the model atmospheric parameters, by varying the stellar parameters by typical uncertainties in the positive direction (i.e., $\Delta T_{\rm eff} = +150$ K, $\Delta \log g = +0.30$ dex, Δ[Fe/H] $= +0.30$ dex, and $\Delta\xi_t = 0.2$ km s^{-1}), and recording the change in abundance. This is shown in Table 5. All changes are within the expected error bars.

4.1. Lithium Abundance in J0524−0336

The lithium abundance was derived from synthesizing the Li lines at 4602, 4971, 6103, 6707, and 8126 Å (atomic data for these lines were adopted from Kramida et al. 2021). We adopted an isotopic ratio of ^{6}Li/^{7}Li = 0. While Lind et al. (2013) measured a negligible ^{6}Li/^{7}Li = 0.005 in two out of four of their Li-rich metal-poor stars, Wang et al. (2022) were not able to detect any ^{6}Li in any of the same stars using higher-resolution ESPRESSO spectra ($R \approx 146{,}000$) and a 3D NLTE analysis. As can be seen in Figure 3, all the Li lines in this star are strikingly strong, with the line at 6707 Å being especially prominent. Li was also detected in the lines at 4273 and 4132 Å, however, as they were blended they were not used in the final abundance average. The five remaining lines yielded lithium abundances of A(4602 Å) = 6.20, A(4973 Å) = 5.90, A(6103 Å) = 6.35, A(6707 Å) = 5.77, and A(8126 Å) = 6.43. The observations and corresponding synthesis of the lines are shown in Figure 3. For comparison, we also show on this figure the same Li lines for two other Li-normal metal-poor stars with similar stellar parameters as J0524−0336. The mere presence of seven detectable lithium lines is highly unusual in such a metal-poor star, as it is more common that only the line at 6707 Å can sometimes be detected, even in Li-rich giants. We note that the 6707 Å resonance line, however, yields a lower Li abundance than the rest of the lines by 0.5 dex. This dispersion can be attributed to the asymmetric nature of this particular line and the strength of its wings. Wang et al. (2021) investigated this (and other) Li line in details using a 3D NLTE analysis. They indicate that as A(Li) increases, the line formation pushes toward higher layers in the stellar photosphere with significantly lower temperatures than deeper layers, which can drive the models away from hydrostatic equilibrium. By excluding the 6707 Å line from the Li average, J0524−0336 yields an abundance of $A(\mathrm{Li})_{\rm 1D,\ LTE} = 6.22$ and $[\mathrm{Li/Fe}]_{\rm 1D,\ LTE} = +7.60$.

NLTE and 3D effects can be substantial for metal-poor giant stars, and particularly for strong Li lines, as is the case in Li-rich stars (Lind et al. 2013; Wang et al. 2021). The A(Li) of J0524–0336 is significantly higher than any existing 3D NLTE Li grid (e.g., Harutyunyan et al. 2018). Therefore, we calculated custom spectra at higher abundances using the same models as described in Wang et al. (2021), interpolated to the derived stellar parameters of J0524−0336. The 3D NLTE best-fit spectral lines to the observations are shown in Figure 4 for the Li lines 6103, 6707, and 8126 Å. Our models do not include computations for the 4602 and 4973 Å lines. We determine an abundance $A(\mathrm{Li})_{\rm 3D,\ NLTE}$ of 6.13 dex and 6.16 dex for the 6103 Å and 8126 Å lines, respectively. On the other hand, the 6707 Å line yields a significantly lower abundance $A(\mathrm{Li})_{\rm 3D,\ NLTE} = 5.38$. As shown in Figure 4, the broad core of this line suggests that it is so strong that it might have formed in the chromosphere, which cannot be fit with our current 3D NLTE models as they are not accounted for in any of our model atmospheres and their implementation is beyond the current scope of the study. Given the excellent fits for the 6103 and 8126 Å lines and the agreement between their abundance values within 0.03 dex, we therefore adopt a final 3D NLTE abundance for J0524−0336 of $A(\mathrm{Li})_{\rm (3D,\ NLTE)} = 6.15$ dex from their average abundances, which

---

[22] https://github.com/vmplacco/linemake

Table 3
Element Abundances in J0524−0336

El.	N	log ϵ (X)$_\odot$	log ϵ(X)	[X/H]	[X/Fe]	σ[X/H]
Li (1D, LTE)	4	1.05	6.22	+5.17	+7.60	0.25
Li (3D, NLTE)	2	1.05	6.15	+5.10	+7.64	0.20
CH	1	8.43	5.70	−2.73	−0.13	0.20
CH (corr.)[a]	1	8.43	6.34	−2.09	+0.51	0.20
O I	1	8.69	7.41	−1.28	+0.99	0.20
Na I (1D, LTE)	1	6.24	5.26	−0.98	+1.30	0.20
Na I (1D, NLTE)	1	6.24	5.06	−1.18	+1.10	0.20
Mg I (1D, LTE)	7	7.60	5.70	−1.90	+0.37	0.19
Mg I (1D, NLTE)	7	7.60	5.75	−1.85	+0.42	0.19
Al I (1D, LTE)	1	6.45	3.53	−2.92	−0.64	0.20
Al I (1D, NLTE)	1	6.45	4.03	−2.42	−0.14	0.20
Si I	2	7.51	5.93	−1.58	+0.69	0.17
K I (1D, LTE)	2	5.03	3.27	−1.76	+0.51	0.06
K I (1D, NLTE)	2	5.03	2.57	−2.46	−0.21	0.06
Ca I (1D, LTE)	21	6.34	4.21	−2.13	+0.15	0.21
Ca I (1D, NLTE)	21	6.34	4.31	−2.03	+0.25	0.21
Sc II	11	3.15	1.11	−2.04	+0.24	0.28
Ti II	43	4.95	3.05	−1.90	+0.38	0.35
Cr I	16	5.64	3.18	−2.46	−0.19	0.17
Mn I	4	5.43	2.88	−2.55	−0.27	0.37
Fe I	178	7.50	5.24	−2.26	+0.01	0.36
Fe II	17	7.50	5.11	−2.39	−0.12	0.15
Co I	3	4.99	2.75	−2.24	+0.04	0.10
Ni I	16	6.22	3.77	−2.45	−0.18	0.30
Zn I	2	4.56	2.03	−2.53	−0.25	0.03
Sr	2	2.87	0.42	−2.45	+0.10	0.29
Y	15	2.21	−0.19	−2.40	+0.14	0.08
Zr	12	2.58	0.46	−2.12	+0.43	0.20
Nb	1	1.46	<0.18	<−1.28	<+1.27	0.30
Mo	1	1.88	<−0.17	<−2.05	<+0.50	0.30
Ru	1	1.75	<0.30	<−1.45	<+1.10	0.30
Rh	1	0.91	<0.56	<−0.35	<+2.20	0.20
Pd	1	1.57	<0.67	<−0.90	<+1.66	0.30
Ag	1	0.94	<0.04	<−0.90	<+1.65	0.30
Ba	5	2.18	0.08	−2.10	+0.47	0.10
La	19	1.10	−0.64	−1.74	+0.81	0.12
Ce	12	1.58	−0.48	−2.06	+0.49	0.09
Pr	9	0.72	−0.74	−1.46	+1.09	0.08
Nd	26	1.42	−0.32	−1.74	+0.81	0.13
Sm	10	0.96	−0.48	−1.44	+1.13	0.09
Eu	12	0.52	−0.69	−1.21	+1.34	0.10
Gd	7	1.07	−0.42	−1.49	+1.07	0.09
Dy	12	1.10	−0.28	−1.38	+1.18	0.11
Ho	1	0.48	<−0.85	<−1.33	<+0.92	0.3
Er	7	0.92	−0.49	−1.41	+1.16	0.36
Tm	2	0.10	−1.15	−1.25	+1.30	0.14
Lu	1	0.10	<−1.05	<−1.15	<+1.40	0.10
Hf	3	0.85	−0.73	−1.58	+0.99	0.06
Ir	1	1.38	<0.03	<−1.35	<+1.22	0.30
Pb	1	1.75	<−0.20	<−1.95	<+0.62	0.30
Th	2	0.02	−1.28	−1.30	+1.27	0.21
U	1	−0.54	<−0.99	<−0.45	<+2.12	0.20

Note.
[a] Following Placco et al. (2014).

renders [Li/Fe]$_{(3D,\ NLTE)}$ = +7.64 (adopting a solar lithium abundance A(Li)$_\odot$ = 1.05; Asplund et al. 2009).

We compare the Li abundance in J0524−0336 to other Li-rich stars in the literature, as shown in Figure 5. To the best of our knowledge, both A(Li) and [Li/Fe] in J0524−0336 are significantly higher than any other Li-rich star reported in the literature to date. It can be seen in Figure 5 that the next highest lithium-enhanced giant, TYC 429-2097-1 (Yan et al. 2018), has A(Li, LTE) = 4.63 and is at a much higher metallicity ([Fe/H] = −0.36) than our star. Thus, J0524−0336 is the first star ever discovered to have an a lithium abundance of A(Li) > 5 and [Li/Fe] > +6 at such a low metallicity. This significant enhancement relative to other Li-rich MW stars suggests a novel or different method of lithium accretion or

Table 4
Line-by-line Element Abundances

λ (Å)	Species	χ (eV)	log *gf*	EW (mÅ)	log ϵ(X) (dex)
6300.30	O I	0.00	−9.82	30.15	7.41
4167.27	Mg I	4.35	−0.71	65.42	5.51
4571.09	Mg I	0.00	−5.68	135.03	6.09
4702.99	Mg I	4.33	−0.38	105.49	5.60
5172.68	Mg I	2.71	−0.45	310.27	5.70
5183.60	Mg I	2.72	−0.23	363.18	5.70
5528.40	Mg I	4.34	−0.49	118.84	5.78
5711.09	Mg I	4.34	−1.72	21.35	5.51
3961.52	Al I	0.01	−0.34	170.81	<3.53
4102.93	Si I	1.91	−3.14	131.52	6.10
5708.39	Si I	4.93	−1.47	16.96	5.76
7664.90	K I	0.00	0.13	112.55	3.32

(This table is available in its entirety in machine-readable form in the online article.)

Table 5
Abundance Uncertainties Due to Fundamental Atmospheric Stellar-parameter Uncertainties

El.	Δ T_{eff} ($\pm\sigma$)	Δ log *g* ($\pm\sigma$)	Δ ξ_t ($\pm\sigma$)	Δ[Fe/H] ($\pm\sigma$)
Li	±0.33	±0.10	±0.01	±0.10
O I	±0.09	±0.03	±0.01	±0.03
Mg I	±0.15	±0.07	±0.03	±0.02
Al I	±0.21	±0.12	±0.03	±0.07
Si I	±0.11	±0.05	±0.02	±0.03
K I	±0.14	±0.03	±0.02	±0.01
Ca I	±0.12	±0.03	±0.01	±0.02
Sc II	±0.03	±0.05	±0.03	±0.01
Ti II	±0.02	±0.03	±0.03	±0.01
Cr I	±0.21	±0.05	±0.03	±0.03
Mn I	±0.22	±0.06	±0.02	±0.04
Fe I	±0.19	±0.05	±0.03	±0.03
Fe II	±0.04	±0.06	±0.02	±0.02
Co I	±0.22	±0.09	±0.05	±0.09
Ni I	±0.15	±0.04	±0.01	±0.02
Zn I	±0.03	±0.03	±0.00	±0.01

production within J0524−0336, or a similar process occurring on extremely short timescales.

4.1.1. Carbon and Oxygen

We derive O abundance from the forbidden [O I] line at 6300 Å. While this line is commonly found to be weak, and often blended with a telluric feature in metal-poor stars, we find a very good fit and derive [O/Fe] = 0.99. We derive the C abundance in J0524−0336 by fitting the CH *G* band at 4313 Å following Masseron et al. (2014). We estimate a carbon abundance of $A(\mathrm{C}) = 5.7$ and a ratio relative to metallicity of [C/Fe] = −0.13. As can be seen in Figure 7, this is not unusual compared to other low-metallicity halo stars from Yong et al. (2013) and Roederer et al. (2014). We were unable to fit the weak NH band between 3355 and 3365 Å, and thus could not estimate an N abundance.

The $^{12}\mathrm{C}/^{13}\mathrm{C}$ isotopic ratio is a strong indicator of the extent of mixing processes in the RGB stage of stellar evolution (Charbonnel et al. 1998; Charbonnel & Zahn 2007). To derive this ratio, we fix the carbon abundance derived from the 4313 Å feature to $A(\mathrm{C}) = 5.7$, and derive $^{12}\mathrm{C}/^{13}\mathrm{C} = 10 \pm 3$ from the 4217 Å line. The best fit syntheses to the CH lines and isotopic ratios are shown in Figure 6. This value suggests substantial processing of $^{12}\mathrm{C}$ into $^{13}\mathrm{C}$ in J0524−0336. Carbon is usually depleted throughout the lives of giant stars. We thus determine and correct for the evolutionary depletion of C due to processing in J0524−0336. We determine a correction of 0.64 dex using the online tool[23] described in Placco et al. (2014). This renders a final [C/Fe] = +0.51, which classifies J0524−0336 slightly below being a carbon-enhanced metal-poor star ([C/Fe] > 0.7).

4.1.2. Light Elements

In addition to Li, C, and O, we also derive light-element ($Z < 30$) abundances of Na, Mg, Al, Si, K, Ca, Sc, Ti, Cr, Mn, Co, Ni, and Zn for J0524−0336, following our abundance analysis of light elements described in Ezzeddine et al. (2020). The derived abundances are listed in Table 3, and are compared to other MW field stars from Yong et al. (2013) and Roederer et al. (2014) in Figure 7.

As already mentioned above, NLTE corrections can be important for nondominant species in the atmospheres of metal-poor giant stars. We thus investigate NLTE corrections for several elements, when available from the `INSPECT` database (Lind et al. 2011). We determine an average NLTE correction for Na I of −0.2 dex from the seven Na I lines we detected in J0524−0336. We derive a −0.7 dex NLTE correction for the K I line at 7698 Å from Takeda et al. (2002). Similarly, we interpolate NLTE corrections for our Mg I abundance from Osorio et al. (2015), and we find a negligible average correction of <0.05 dex for J0524−0336. For Al I, we determine the abundance from the 3961 Å line, which is heavily affected by NLTE in cool metal-poor stars (Nordlander & Lind 2017). We estimate an NLTE correction of ~0.5 dex based on their published grids and the stellar parameters of J0524−0336. Finally, we estimate an ~0.1 dex NLTE correction for Ca I from Mashonkina et al. (2016). For consistency of comparison with the literature abundances, derived in LTE, we only show our LTE abundances of J0524−0336 in Figure 7, however, we list both the LTE and NLTE values whenever relevant in Table 3.

The abundances of all light elements ($Z < 30$) in J0524−0336 agree with the trends typically observed in metal-poor MW halo stars, except for Na, which seems to be enhanced related to the MW stars, with [Na/Fe] (1D, LTE) = +1.30. Additionally, both Ni and Zn seem to be low as compared to the MW field stars. We note that no connection between the peculiarity of the abundances of these elements and the Li enhancement has, however, been established. Our element abundance derivations also agree well with those derived for J0524−0336 in Ezzeddine et al. (2020).

4.2. Neutron-capture Element Abundances

We also measure abundances of neutron-capture elements in our star. J0524−0336 was originally identified and classified as a highly enhanced *r*-II star ([Eu/Fe] > +0.7; Holmbeck et al. 2020) in Ezzeddine et al. (2020), from measurements of Sr, Ba, and Eu abundances. We rederived the abundances of these elements, in addition of other neutron-capture elements from our high-resolution, high-S/N spectrum. The Eu abundance

---

[23] http://vplacco.pythonanywhere.com/

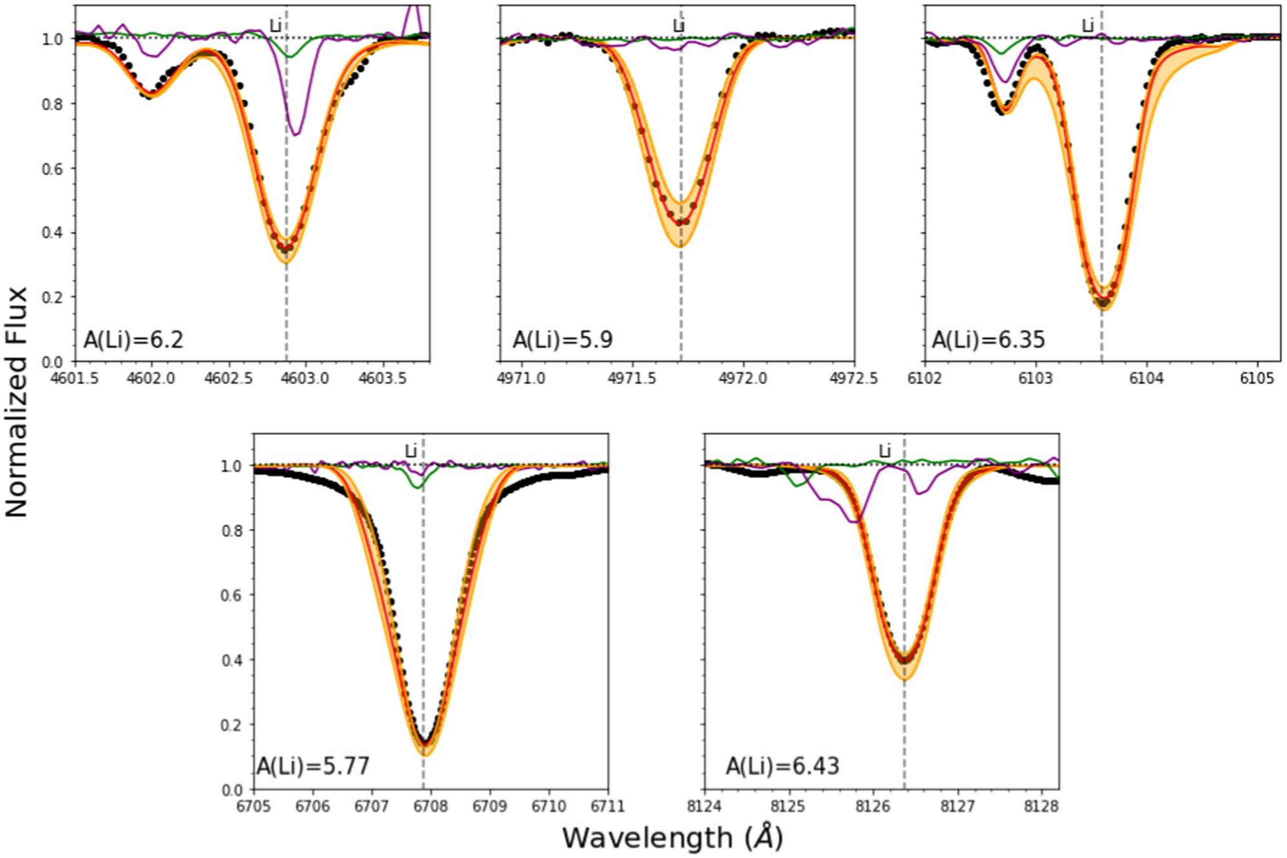

Figure 3. Line profile observations, as well as 1D LTE synthetic spectral fits for the five strong lithium lines detected in J0524−0336. The $\pm\sigma = 0.25$ abundance fits are also shown in the shaded orange. For comparison, we display the same Li lines for the two metal-poor stars at similar [Fe/H] as J0524−0336, HE 0048−1109 (purple) with $A(\mathrm{Li}) = 2.34$, and HE 0324−0122 (green) with $A(\mathrm{Li}) = 0.78$.

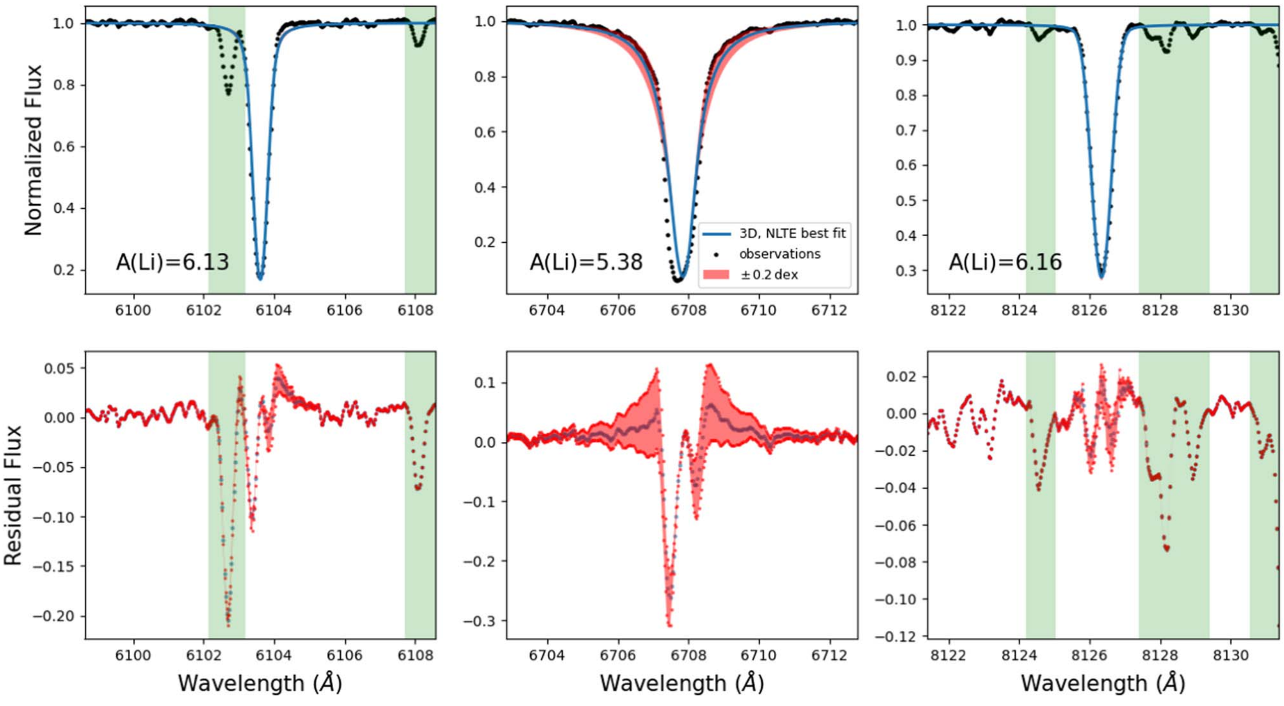

Figure 4. Upper panel: spectral line observations (black dots) and 3D NLTE fits (blue lines) for the Li lines at 6103 Å, 6707 Å, and 8126 Å, respectively. The red shaded area shows the spectral lines at ±0.2 dex from the best fits. Lower panel: residuals between the observed flux and best-fit flux (blue points), as well as the ±0.2 dex spectra from the best fit (red shaded area). The vertical green shaded areas in both panels show the masked lines excluded from the fits.

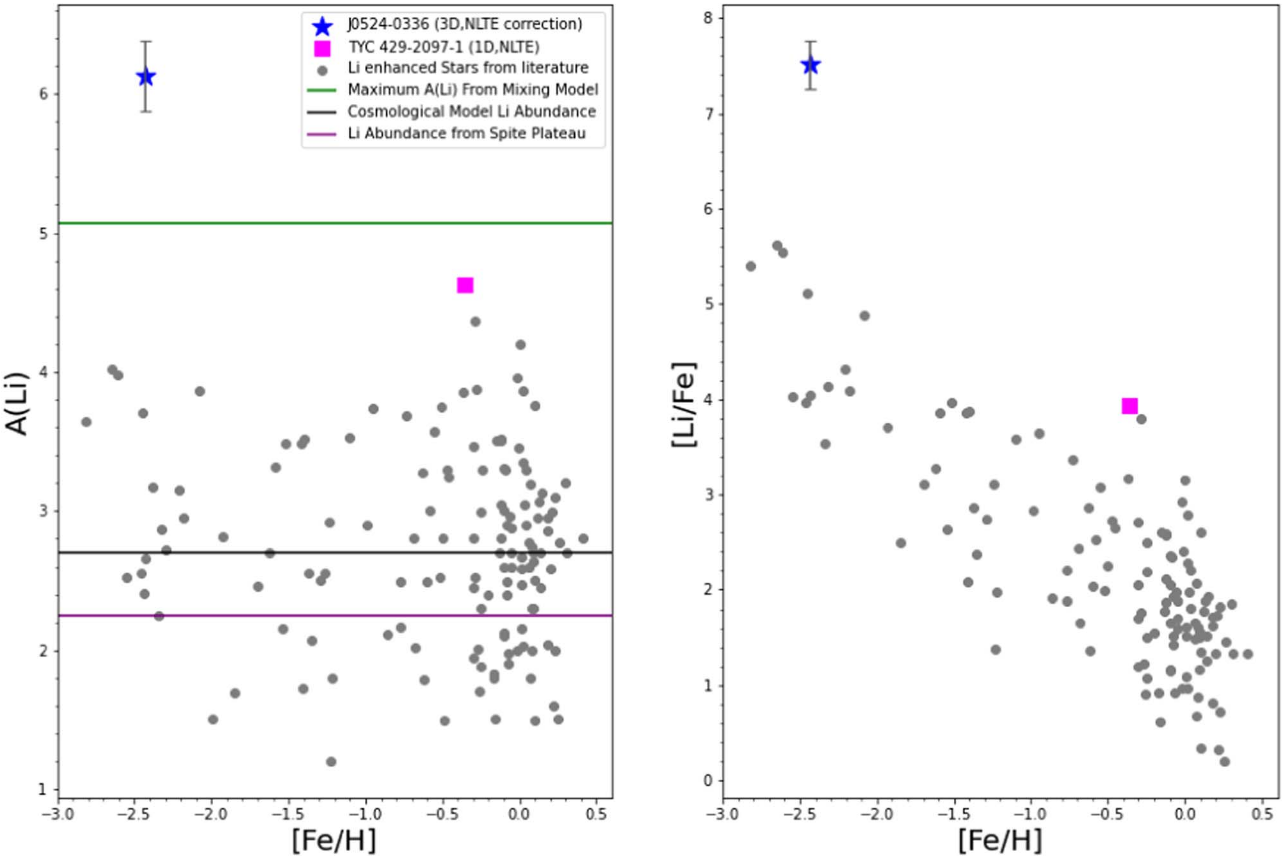

Figure 5. Absolute lithium abundance, A(Li) (left panel) and [Li/Fe] (right panel) plots for J0524−0336 (derived using 1D LTE and 3D NLTE corrected values in red and blue stars, respectively) vs. [Fe/H], and other lithium-rich giant stars from the literature. The star with the next highest Li abundance after J0524−0336, TYC 429-2097-1 (Yan et al. 2018), is also shown on the plots by the magenta square. The primordial cosmological Li abundance (black line), the Spite Plateau (magenta line), as well as the maximum Li enhancement from mixing models (green line) from Yan et al. (2018) are also shown. References are Wallerstein & Sneden (1982), Luck (1982), Hanni (1984), Brown et al. (1989), Gratton & D'Antona (1989), McWilliam & Rich (1994), Carney et al. (1998), Jasniewicz et al. (1999), Andrievsky et al. (1999), Hill & Pasquini (1999), Smith et al. (1999), Balachandran et al. (2000), Reyniers & Van Winckel (2001), Drake et al. (2002), Canto Martins et al. (2006), Gonzalez et al. (2009), Lèbre et al. (2009), Carlberg et al. (2010, 2015), Monaco et al. (2011, 2014), Alcalá et al. (2011), Kumar et al. (2011), Ruchti et al. (2011), Kirby et al. (2012, 2016), Anthony-Twarog et al. (2013), Martell & Shetrone (2013), Liu et al. (2014), Adamów et al. (2014, 2015), D'Orazi et al. (2015), Jofré et al. (2015), Casey et al. (2016), and Yan et al. (2018).

was derived from 12 Eu II lines, which rendered $A(\mathrm{Eu}) = -0.69 \pm 0.10$ and $[\mathrm{Eu/Fe}] = +1.34 \pm 0.10$. This agrees with the value derived in Ezzeddine et al. (2020). We also derive $[\mathrm{Ba/Fe}] = +0.47 \pm 0.10$, with $[\mathrm{Ba/Eu}] = -0.87 \pm 0.20$, suggesting a major contribution of neutron-capture elements in J0524−0336 from an r-process origin. It is worth noting that this r-process enhancement is unlikely to be related to the Li enhancement in J0524−0336.

In addition to Eu and Ba, we measure abundances for Sr, Y, Zr, La, Ce, Pr, Nd, Sm, Gd, Dy, Er, Tm, Hf, and Th, as well as upper limits for Nb, Mo, Ru, Rh, Pd, Ag, Tb, Lu, Ir, Pb, and U. Figure 8 shows the neutron-capture abundance pattern for J0524−0336 with the scaled solar r-process pattern relative to Eu and the scaled s-process pattern relative to Ba from Sneden et al. (2008). The abundance patterns of J0524−0336 closely match that of the scaled r-process, except for Sr and Y from the first r-process peak, which is consistent with the abundances of these elements derived in other r-process enhanced stars, indicating the possible onset of a weak, secondary r-process origin (e.g., Hansen et al. 2012).

5. Stellar Evolutionary Status of J0524−0336

To understand the ultraLi enhancement in J0524−0336 ($A(\mathrm{Li}) > 5$), it is crucial to establish its evolutionary status. We compute tailored stellar-evolution models using the latest version of the stellar-evolution code STAREVOL (see Dumont et al. 2021b for references and details on the equation of state, opacities, and nuclear reactions). The initial chemical composition accounts for the values of [Fe/H], [C/Fe], [O/Fe], and [Na/Fe] derived in this work (see Section 4 and Table 3 for values). We use a gray atmosphere and define the stellar effective temperature and radius at the optical depth $\tau = 2/3$. The mass-loss rate follows Reimers (1975)'s empirical relation (with $\eta_R = 0.5$) from the zero-age main sequence up to central He exhaustion and switches to Vassiliadis & Wood (1993)'s prescription on the AGB. We adopt a mixing length parameter $\alpha_{\mathrm{MLT}} = 1.5$, and we assume the Schwarzschild criteria for convective stability. We include the effects of thermohaline instability as described in Charbonnel & Zahn (2007) and Lagarde et al. (2012). We also compute models with thermohaline mixing and solid-body rotation, to predict the evolution of the surface stellar rotation rate under conservative assumptions for such a low-mass star.

The position of J0524−0336 on the H-R diagram and on the Kiel diagram is well fit by the evolutionary track of a model with initial mass of 0.8 $M_\odot$ (see Figure 9). Given the uncertainties on the stellar parameters, J0524−0336 appears to be located either on the RGB above the predicted location of

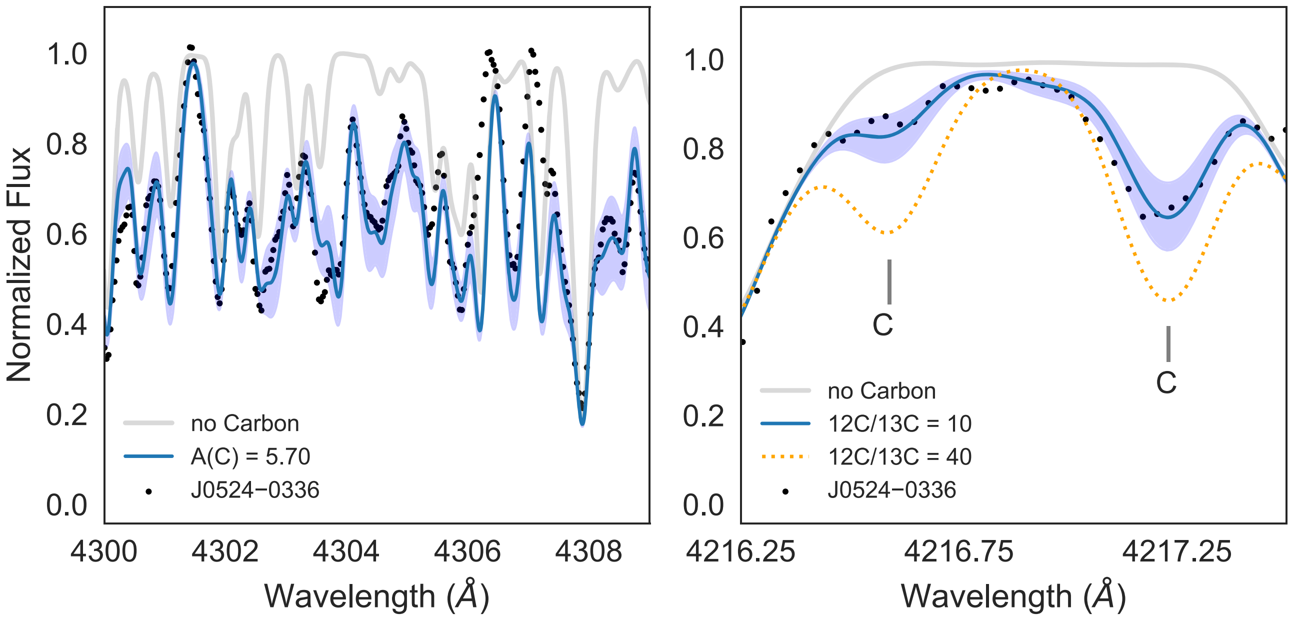

Figure 6. Left panel: spectral synthesis of the CH *G* band for J0524−0336. The filled black circles represent the observed high-resolution spectrum, the solid blue is the best abundance fit, and the blue shaded area encompasses a 0.2 dex difference in *A*(C). The light-gray line shows the synthesized spectrum in the absence of carbon. Right panel: determination of the carbon isotopic ratio, $^{12}\mathrm{C}/^{13}\mathrm{C}$. The filled circles represent the observed spectrum, the solid blue line is the best fit for $^{12}\mathrm{C}/^{13}\mathrm{C} = 10$, and the dashed orange line is for $^{12}\mathrm{C}/^{13}\mathrm{C} = 40$. The blue shaded area encompasses a 0.2 dex difference in *A*(C). The light-gray line shows the synthesized spectrum in the absence of carbon.

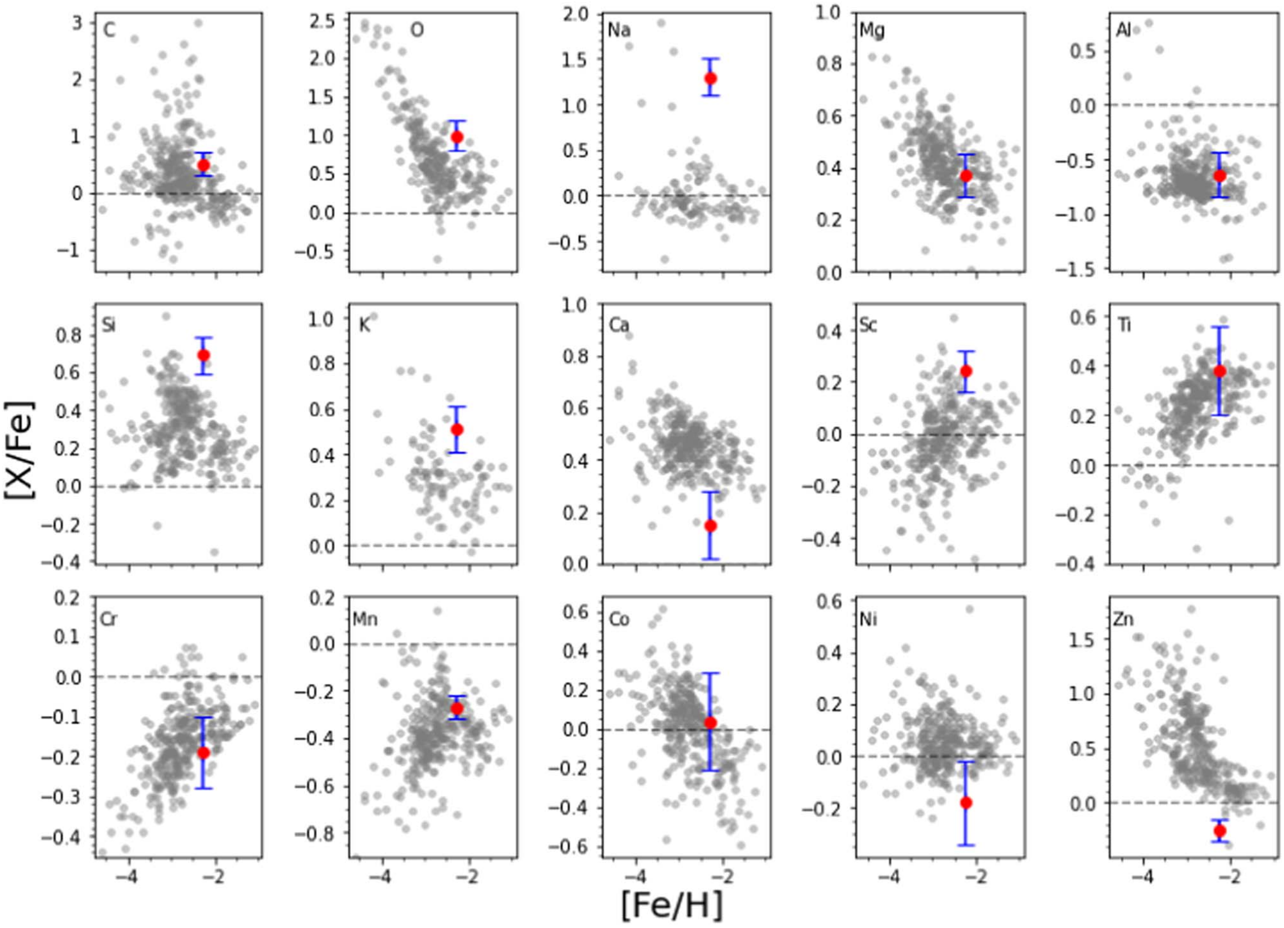

Figure 7. The [X/Fe] abundance ratios of C through Zn in J0524−0336, compared to MW halo stars from Yong et al. (2013) and Roederer et al. (2014).

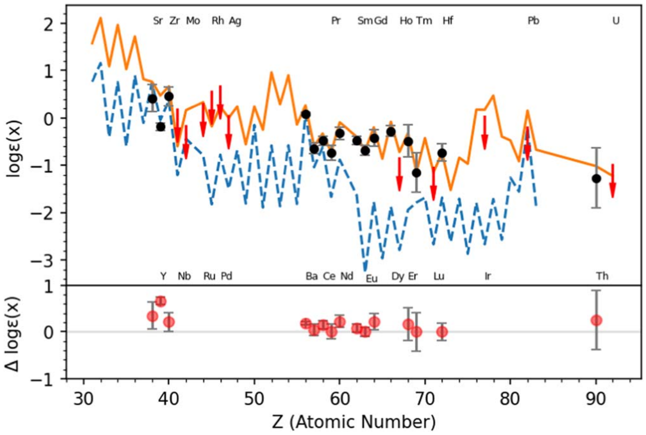

Figure 8. Derived neutron-capture abundances (black circles), as well as upper limits (red downward arrows) in J0524−0336 overplotted against the scaled solar *r*-process (orange solid line) and *s*-process (blue dashed line) abundance patterns from Sneden et al. (2008). The lower panel shows the residual plot for the abundances we measured with respect to the solar *r*-process pattern.

the bump, or on the early AGB (e-AGB) before the occurrence of the thermal pulses on the AGB (TP-AGB). It has a much cooler temperature than the position of the horizontal branch (HB), which is the metal-poor counterpart of the RC for metal-rich giants. Although no asteroseismic constraint is available for J0524−0336, we can safely conclude that it is currently *not* undergoing central He burning.

We computed different global asteroseismic quantities (ν max, frequency at which the oscillation modes reach their strongest amplitudes, $\Delta\Pi$, asymptotic period spacing of g-modes (for $l = 1$), total acoustic radius, and acoustic radius at the base of the convective envelope) all along the evolution with the same prescriptions as in Lagarde et al. (2012). At the two evolutionary points on the RGB and e-AGB where our model reaches the luminosity of J0524–0336 and has an effective temperature compatible with the derived values within the error bars, their values are very similar, and 2–3 orders of magnitude lower than when the model undergoes central He burning at a very high effective temperature on the HB (see Lagarde et al. 2012 for a description of the variations of the global asteroseismic quantities along the evolution of low-mass stars from the pre–main sequence to the end of the TP-AGB).

Within the error bars on the luminosity and effective temperature of J0524−0336, both on the RGB and the e-AGB, the model predicts a value of 9.6 for the $^{12}\mathrm{C}/^{13}\mathrm{C}$ ratio (to compare to the value of 42 obtained after the first dredge-up), due to the effect of the thermohaline mixing that is predicted to occur at the RGB bump. This is in very good agreement with the value we derived of $^{12}\mathrm{C}/^{13}\mathrm{C} = 10$, confirming that J0524−0336 has already undergone thermohaline mixing when it has previously crossed the RGB bump. The typical rotation rate for stars at this evolution stage and metallicity is 1.2 km s^{-1} (Cortés et al. 2009), which is much lower than that derived in this study (see Section 3.5).

6. Discussion

The evolutionary status of Li-rich giants has long been debated. Charbonnel & Balachandran (2000) found an accumulation of such stars around the RGB bump and on the e-AGB, this later phase being in agreement with our conclusions for J0524−0336. Interestingly, the next most highly enhanced lithium star ($A(\mathrm{Li}) = 4.51$) is probably located at the RGB bump (Yan et al. 2018). Others studies, sometimes using additional constraints based on asteroseismology parameters, concluded that a large fraction of enhanced lithium giants are actually RC stars presently burning He in their central convective core, the rest being either close to the RGB bump or randomly distributed along the advanced phases (Kumar et al. 2011; Silva Aguirre et al. 2014; Casey et al. 2019; Kumar & Reddy 2020; Yan et al. 2020, 2021; Martell et al. 2021). Recent studies have shown that there could be different paths to Li enrichment. For example, Chanamé et al. (2022) demonstrated that lithium-rich RC giants are likely to be a younger and more massive population than lithium-rich RGB stars. Sayeed et al. (2024) performed an empirical study of Li-rich giants from the GALAH survey and showed that while Li-rich stars are prevalent on the RC, other culprits such as binary spin-up and mass transfer could also be likely mechanisms to enrich stars with Li at the RGB phase. As of today, though, there is still no clear consensus, and different paths to Li enrichment remain to be explored and confirmed observationally.

Several mechanisms have been suggested in the literature to try to explain Li richness in giant stars. These can be broadly divided into external and internal mechanisms. External mechanisms include the presence or interaction with a stellar or substellar companion (such as planetary engulfment or binary interactions), while internal mechanisms include non-traditional or enhanced mixing processes. In what follows, we discuss some of these different mechanisms, linking them to the observable properties of J0524−0336, to try to explain its extreme lithium enhancement relative to other stars in the MW.

6.1. External Enrichment

6.1.1. Planetary Engulfment

One mechanism that has been proposed for lithium enhancement in giant stars is planetary engulfment (Siess & Livio 1999). Planets below a certain mass threshold can dissolve in the convective envelope of a host star, which can (in some cases) lead to lithium (as well as other elemental) enhancement, and is postulated to be observed in the photospheric abundances of giant stars with $1.5 \leqslant A(\mathrm{Li}) \leqslant 2.2$. Aguilera-Gómez et al. (2016) have attempted to model lithium enrichment via the engulfment of a planet or a brown dwarf across a range of stellar metallicities and substellar component masses, where they showed that planetary engulfment is unable to account for giant stars with $A(\mathrm{Li}) \geqslant 2.2$. This has been further confirmed by a follow-up study (Aguilera-Gómez et al. 2020). It is unlikely that a star at such a low metallicity as J0524−0336 would be able to form a planet (Fischer & Valenti 2005), however, as an academic exercise, we nevertheless attempt to derive the substellar component parameters (including the mass and initial Li abundance) that would be theoretically required to account for the Li abundance in J0524−0336. We adopt the equations in Carlberg et al. (2012, see their appendix), starting with a star of similar mass to J0524−0336 (0.8 $M_\odot$) to estimate the Li abundance the star would have after the substellar component engulfment event. We adopt a ratio of the mass of the planet to the mass of the stellar envelope of 0.19, with the mass of the envelope being 0.05 the mass of the star. This would result in a planet of size 8 M_J, although we allowed the mass and thus the former ratio to vary from 1 to 32 M_J (thus the ratio of the mass of the planet to the

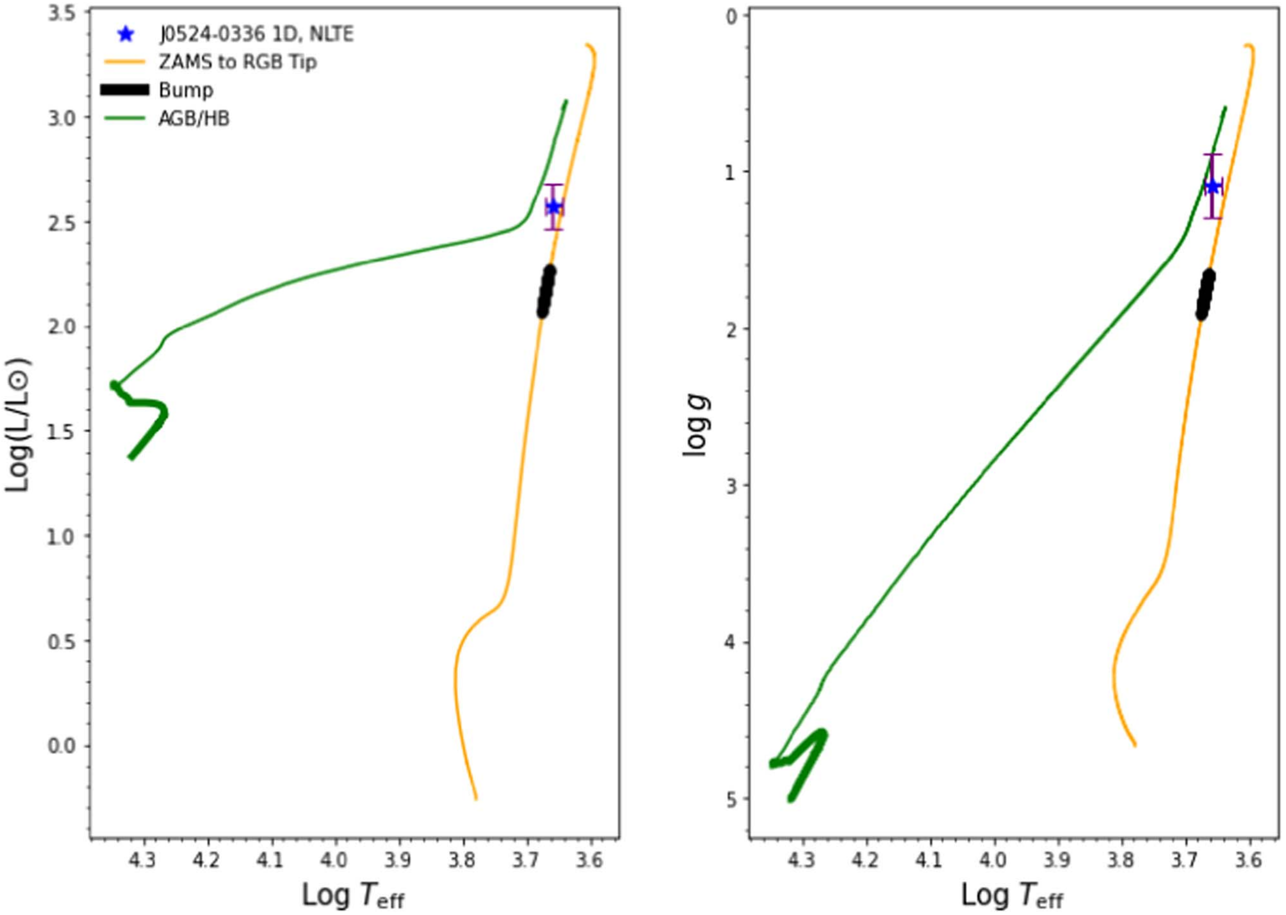

Figure 9. J0524−0336 overplotted on the stellar evolutionary track in the H-R diagram and the Kiel diagram (left and right panels, respectively) of a 0.8 $M_\odot$ model computed with the initial [Fe/H], [C/Fe], [O/Fe], and [Na/Fe] of J0524−0336. Different stellar evolutionary phases are highlighted on each diagram. The orange line goes from the zero-age main sequence up to the RGB tip, and the green one from the zero-age HB to the occurrence of the first TP-AGB. The RGB bump (black bold), and the location where central He burning occurs on the HB (bold green) are also shown on the plots.

stellar envelope varies from 0.02 to 0.76). We show the results in Figure 10. The left panel shows the "final" expected Li abundance of the star, starting with an "initial" Li abundance of $A(\mathrm{Li}) = 2.2$, after engulfing a planet with different intrinsic Li abundances, ranging from $A_p(\mathrm{Li}) = 3.3$ to 7.5, as a function of planet mass (in units of M_J). The right panel of Figure 10 shows the same thing, however, starting from a highly enriched "intrinsic" stellar Li abundance of $A(\mathrm{Li}) = 4.0$, for example, a star that has been previously enriched by an internal mixing process. According to the the models outlined in Carlberg et al. (2012), regardless of the "initial" stellar Li abundances ($A(\mathrm{Li}) = 2.2$ and $A(\mathrm{Li}) = 4.0$), the "final" stellar photospheric Li abundances are expected to increase as a function of planet mass and intrinsic planetary Li content. For both cases, however, an unrealistically high intrinsic planetary Li content ($A_p(\mathrm{Li}) > 7.0$) is needed to reproduce the Li abundance in J0524−0336. Additionally, it would take a large planet ($\geqslant 10\ M_J$) to account for this level of Li enrichment in J0524−0336. Both scenarios seem unlikely, given our current understanding of intrinsic planetary lithium content. We can thus dismiss planetary engulfment as a primary mechanism of Li enrichment in J0524−0336.

6.1.2. Interaction with a Binary Stellar Companion

The presence and interaction with a binary companion has been proposed as a scenario to explain lithium enhancement in stars. For example, Casey et al. (2019) proposed that tidal interactions from a companion star could create internal mixing and thus drive lithium enhancement via the Cameron & Fowler (1971) mechanism. It has also been proposed by Zhang et al. (2020) and Mallick et al. (2022) that lithium enhancement could result from mergers between RGB stars and helium white dwarf companions, where the surface Li abundance would get enhanced during the common envelope phase of the merger during the inspiraling of the binary components, which would eventually lead to the formation of a Li-rich He-burning core RC star.

We derived the RV of J0524−0336 (as explained in detailed in Section 2) from three different spectroscopic observational epochs of J0524−0336 over several years, and compared it to the Gaia DR3 RV. We found an excellent agreement within <2 km s^{-1}, which excludes any RV variation. Additional insight on RV variation can be obtained by looking at the renormalized unit weight error (RUWE) from the Gaia database, which corresponds to the reduced chi-squared of the best-fitting five-parameter single-body astrometric solution. Lindegren et al. (2021) suggested that a RUWE value >1.4 could be used to signal and identify possible nonsingle stars. J0524−0336 has a RUWE value of 1.02, which further excludes at the present any evidence for a binary companion.

Nevertheless, Hα emission profile changes and IR excesses have been suggested to be due to binary mergers that trigger mass-loss events (Castellani & Castellani 1993; Zhang & Jeffery 2013). In this case, excess in near-infrared colors will

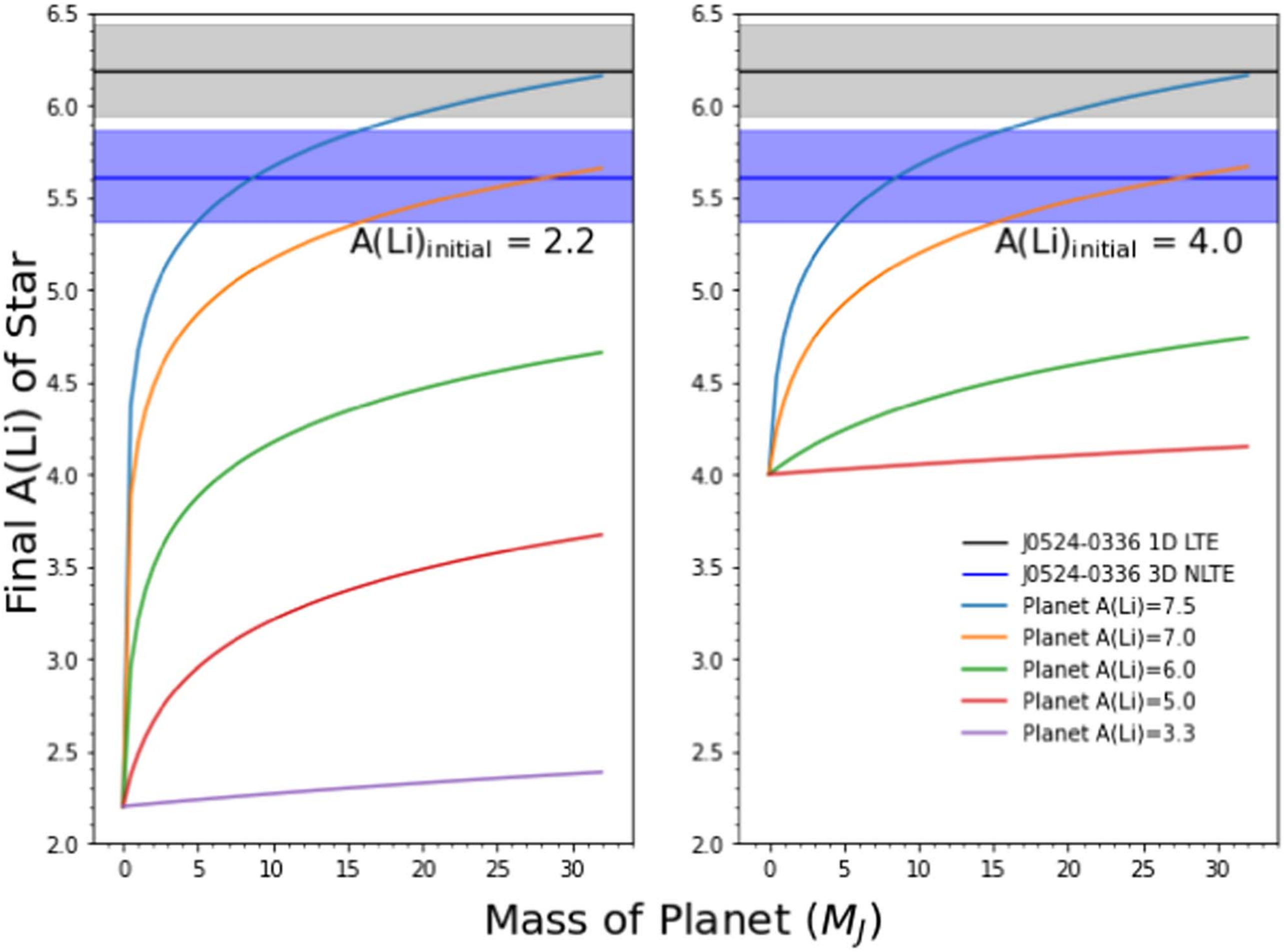

Figure 10. Final Li abundance after a theoretical planetary engulfment event, based on models from from Carlberg et al. (2012), starting with an initial stellar Li abundance of $A(\mathrm{Li}) = 2.2$ (left panel), and a superhigh initial abundance (possibly due to enhanced internal mixing) of $A(\mathrm{Li}) = 4.0$ (right panel), as a function of planet mass. It should be noted that the deuterium burning limit is at 13 M_J and thus “planets” larger than this might more realistically be considered brown dwarfs.

be detected if the material was ejected recently (Mallick et al. 2022). This signifies the possibility that, while no present binary component has been detected for J0524−0336, it might have experienced a recent binary merger that could have invoked extra mixing, leading to enhanced rotation and mass-loss events, as evidenced by the detection of variable emission in the Hα profile, and first-order IR flux excess.

6.2. Internal Mixing

Lithium production in red giants requires a mechanism to transport ^{3}He inwards from the stellar convective envelope to the deeper and hotter radiation layers where the *pp* II chain produces fresh ^{7}Be, and then to transport ^{7}Be outwards so that its electron capture to ^{7}Li occurs in cooler regions where ^{7}Li cannot burn (the so-called Cameron–Fowler process; Cameron & Fowler 1971). Although the general idea is well understood and several driving mixing processes have been proposed, the physical origin of the transport mechanism is far from being clear.

As initially shown by Sackmann & Boothroyd (1992), the amount of Li that can potentially be produced in evolved stars strongly depends on the assumed speed and geometry of the driving mixing mechanism as well as on its episodicity, and it is independent of the previous ^{7}Li depletion history of the stars. Yan et al. (2018) revisited this seminal work, using updated nuclear reaction rates and asymmetric parameters for the upwards and downwards mixing flows between the base of the convective envelope and the ^{7}Be production layers. Their fine-tuned model was able to reproduce the Li abundance ($A(\mathrm{Li}) = 4.51$) of their star, TYC 429−2097-1, which is more massive and more metal rich ($M = 1.43 \pm 0.55\ M_\odot$, $[\mathrm{Fe/H}] = -0.36 \pm 0.06$) than J0524−0336, and which is lying at the RGB bump (this was established by the authors based on Gaia Data Release 1 parameters, and we checked that it is still the case with Gaia Data Release 2 and Gaia DR3). However, their parametric model only allowed for a maximum lithium abundance of $A(\mathrm{Li}) = 5.07$, which is a factor of ∼4 below that of J0524−0336. We speculate that this small difference could be due to the differences in mass and metallicity between the two stars, calling for the same transport process to be more efficient in more metal-poor giants. This was actually already anticipated based on the observed $^{12}\mathrm{C}/^{13}\mathrm{C}$ behavior along the RGB, which reveals the role of molecular weight gradient in the development of transport processes such as thermohaline mixing in red giants (Charbonnel et al. 1998; Charbonnel & Zahn 2007; Lagarde et al. 2012, 2019).

6.2.1. Lithium Flash

The scarcity of extremely Li-rich red giants like J0524−0336 and TYC 429−2097-1 calls for these stars being caught during a very brief episode at the beginning of the Li-enrichment phase, as originally proposed to occur at the RGB bump and/or during the e-AGB by Charbonnel & Balachandran (2000). The occurrence of this so-called Li flash was first modeled around the RGB bump by Palacios et al. (2001). They suggested that rotation-induced mixing, which they were modeling with a very simplified formalism, would drive the Cameron–Fowler process, leading to the formation a very thin, short-lived, lithium-burning shell in the outskirts of the hydrogen-burning shell. They showed that under certain assumptions for the mixing efficiency, the amount of nuclear energy released in the lithium-burning shell is such that a thermal instability could be ignited. Convection then develops in the thermally unstable layers to carry out the energy, which allows the quasi-instantaneous transport of fresh ^{7}Be toward the convective envelope. During this short-lived ($\sim 2 \times 10^4$ yr) Li flash, the total stellar luminosity temporarily increases by a factor of ∼5 in their model. This causes a near doubling of the mass loss, which could potentially form a dust shell around the lithium-rich star. Once the thermal instability is quenched, the stellar luminosity decreases to its original bump value. The transport efficiency decreases simultaneously, and the stellar envelope is not fed any more with fresh ^{7}Be. The Li abundance and the carbon isotope ratio start to decrease, under, e.g., the influence of thermohaline mixing. Whether this mechanism (which efficiency is strongly debated; see, e.g., Harrington & Garaud 2019, and references therein), or any other instability in rotating stars could be the original trigger of the Li flash at the RGB bump and/or on the e-AGB, remains to be studied.

We see evidence of many aspects of this process in the spectra of J0524−0336 and TYC 429−2097-1: (i) the stars' evolutionary status, as defined by their stellar parameters, is compatible with the two stages at which the lithium flash is expected to occur; we note in particular that the stellar luminosity of J0524−0336 is a factor of ∼5 brighter than the location of the RGB bump predicted by our model, and a factor of ∼2 brighter than the beginning of the e-AGB; TYC 429−2097-1 is at the RGB bump; (ii) the unusually high projected rotational velocity ($v_{\sin i} \sim 11$ km s^{-1} in both J0524−0336 and TYC 429−2097-1) suggests that the transport mechanism simultaneous extracts angular momentum from the stellar interior; (iii) the ^{12}C/^{13}C ∼ 10 ratio in J0524−0336 (12 in TYC 429−2097-1) indicates a decrease below the post-dredge-up value (possibly due to thermohaline mixing) as observed in the majority of bright low-mass red giants; it is also possible that J0524−0336 has acquired its low carbon isotopic value at the RGB bump and is presently undergoing the Li flash on the e-AGB; (iv) the detection of IR-excess colors, as well as the strong and variable emission in the Hα wing profile of J0524−0336, indicates the presence of a dust shell, which could result from enhanced mass loss during the Li flash; we note however that no IR excess was found for TYC 429−2097-1; and (v) the uniquely ultralithium abundance observed in J0524−0336, which requires an extremely efficient transport of ^{7}Be in its convective envelope; the Li abundance of TYC 429−2097-1, which is 1 order of magnitude below that of J0524−0336, is however still 1 order of magnitude above the meteoric value. It is thus possible that both J0524−0336 and TYC 429−2097-1 are indeed just undergoing a lithium flash.

7. Summary and Conclusions

We report on the discovery of J0524−0336, an ultraLi-rich star, with A(Li, 3D, NLTE) = 6.15 and [Li/Fe] = +7.64, from two strong lithium absorption lines. To our knowledge, this is the most Li-rich giant star discovered to date. Additionally, we derive abundances of 16 neutron-capture elements in J0524−0336 with [Eu/Fe] = +1.34, classifying it as a highly enhanced r-process star (r-II; [Eu/Fe] > 0.7; Holmbeck et al. 2020). We conduct a detailed stellar-parameter analysis of our star using a high-resolution ($R \sim 35{,}000$), high-S/N spectrum. Based on its stellar parameters and Gaia DR3 distance, we find that J0524−0336 lies either on the RGB between the bump and the tip, or on the e-AGB. In any case, it is not currently undergoing core He burning, which is predicted to occur at a much higher temperature for such a low-mass, low-metallicity star. The star should thus have a relatively low asymptotic period spacing of g-modes. Additionally, we determine a fast projected rotational velocity, $v_{\sin i} \sim 11$ km s^{-1}, as compared to typical values in red giant stars. Furthermore, both an IR excess as well as variable emission in the wings of the Hα profile were detected.

We investigated both internal and external processes of possible lithium enhancement that might explain such an ultrahigh lithium abundance in a red giant star. A fast rotational velocity could point toward an external source of enrichment, either due to a substellar companion (e.g., planetary) engulfment or binary interaction. No variation was detected in the star's RV over several observational epochs, from which no present binary companion can be inferred. Nevertheless, Hα emission and IR excess have been postulated to be due to mass-loss events due to a binary merger with giant stars. We show that a substellar companion engulfment cannot produce the Li abundance observed in J0524−0336, and that a scenario in which this would be possible would require a high planetary mass ($M_p \geqslant 10$ $M_{\rm J}$) and an unrealistically high intrinsic planetary Li content (A_p(Li) > 7). On the other hand, it could be possible that the ultrahigh Li in J0524−0336 could be due to a previous merger with a binary star triggering and producing extra Li that is then mixed in the star. Additional studies on the exact amount of Li that could be produced during these interactions are, however, needed to confirm or refute such an event in J0524−0336.

We also investigate possible mixing mechanisms that could drive the so-called Cameron–Fowler process in the radiative layers between the H-burning shell and the convective envelope of J0524−0336, and account for its extreme Li abundance. Recent parametric models, taking into account asymmetric upwards and downwards mixing flows and updated nuclear reaction rates, could reach A(Li) = 5.07 for the case of a more massive and more metal-rich red giant sitting at the RGB bump. Similar computations should be done for the case of a low-metallicity, low-mass star such as J0524−0336, to investigate the mass and metallicity dependence of the driving mixing mechanism. We also considered the possibility of Li production in J0524−0336 during the lithium flash as proposed by Palacios et al. (2001), and which is expected to occur at the RGB bump and/or on the e-AGB (Charbonnel & Balachandran 2000). J0524−0336's evolutionary status, fast rotational velocity of $v_{\sin i} \sim 11$ km s^{-1}, IR excess, Hα emission, and unusually high lithium content are predicted indicators of the lithium flash as described in Palacios et al. (2001). It is therefore possible that J0524−0336 was observed during this rare phenomenon, as well as TYC 429-2097-1, which is the next highest $A(\mathrm{Li})$ red giant star, and which is sitting at the bump. However, additional models and upper limits on the production of Li during the Li flash (preferably in 3D), are needed to confirm this scenario.

J0524−0336 sets a new benchmark for lithium-rich metal-poor stars, being the first giant discovered with an $A(\mathrm{Li}) > 6.0$ and $[\mathrm{Li/Fe}] > +7$. It provides a great opportunity to investigate the origin and evolution of Li in the Galaxy, and could be the first of a new population of ultrarich lithium-enhanced stars expected to be discovered in current and future high-resolution spectroscopic surveys such as the RPA, as well as others. Asteroseismologic follow-up of metal-poor Li-rich targets will be key to pin down the exact evolutionary status of our and similar stars. However, distinguishing whether J0524−0336 is climbing the RGB or the e-AGB would be extremely challenging, since the global asteroseismic parameters should not differ significantly between these two evolution phases. Finally, we hope that the discovery of J0524−0336 will open a new avenue to understand the instabilities that can develop and transport matter and angular momentum in red giant stars.

Acknowledgments

We thank Laurent Eyer, Peter Hoeflich, and Pavel Dennisenkov for very helpful discussions. J.K. thanks the University of Florida and the Center for Undergraduate Research and the University Scholars Program for funding his research. R.E. acknowledges support from NSF grant AST-2206263. C.C. acknowledges support by the Swiss National Science Foundation (Project 200020-192039) and thanks N. Lagarde for useful discussions. I.U.R. acknowledges support from the NSF, grants AST 1815403/1815767 and 2205847, and the NASA Astrophysics Data Analysis Program, grant 80NSSC21K0627. A.F. acknowledges support from NSF grant AST-1716251. We acknowledge support from JINA-CEE (Joint Institute for Nuclear Astrophysics—Center for the Evolution of the Elements), funded by the NSF under grant No. PHY-1430152. The work of V.M.P. is supported by NOIRLab, which is managed by the Association of Universities for Research in Astronomy (AURA) under a cooperative agreement with the National Science Foundation. T.T.H. acknowledges support from the Swedish Research Council (VR 2021-05556). This work was supported by computational resources provided by the Australian Government through the National Computational Infrastructure (NCI) under the National Computational Merit Allocation Scheme, the ANU Merit Allocation Scheme (project y89), and an HPC-AI Talent Programme Scholarship (project hl99).

This work made use of NASA's Astrophysics Data System Bibliographic Services, and the SIMBAD database, operated at CDS, Strasbourg, France (Wenger et al. 2000). This work has made use of data from the European Space Agency (ESA) mission Gaia (https://www.cosmos.esa.int/gaia), processed by the Gaia Data Processing and Analysis Consortium (DPAC; https://www.cosmos.esa.int/web/gaia/dpac/consortium).

Facility: Magellan-Clay.

Software: IRAF (Tody 1993), matplotlib (Hunter 2007), MOOG (Sneden 1973; Sobeck et al. 2011), and LOTUS (Li & Ezzeddine 2022).

ORCID iDs

Jeremy Kowkabany https://orcid.org/0000-0001-9566-4237
Rana Ezzeddine https://orcid.org/0000-0002-8504-8470
Corinne Charbonnel https://orcid.org/0000-0002-6449-6194
Ian U. Roederer https://orcid.org/0000-0001-5107-8930
Yangyang Li https://orcid.org/0000-0002-9953-7929
Zoe Hackshaw https://orcid.org/0000-0002-3855-3060
Timothy C. Beers https://orcid.org/0000-0003-4573-6233
Anna Frebel https://orcid.org/0000-0002-2139-7145
Terese T. Hansen https://orcid.org/0000-0001-6154-8983
Erika Holmbeck https://orcid.org/0000-0002-5463-6800
Vinicius M. Placco https://orcid.org/0000-0003-4479-1265
Charli M. Sakari https://orcid.org/0000-0002-5095-4000

References

Adamów, M., Niedzielski, A., Villaver, E., et al. 2015, A&A, 581, A94
Adamów, M., Niedzielski, A., Villaver, E., Wolszczan, A., & Nowak, G. 2014, A&A, 569, A55
Aguilera-Gómez, C., Chanamé, J., & Pinsonneault, M. H. 2020, ApJL, 897, L20
Aguilera-Gómez, C., Chanamé, J., Pinsonneault, M. H., & Carlberg, J. K. 2016, ApJ, 829, 127
Aguilera-Gómez, C., Monaco, L., Mucciarelli, A., et al. 2022, A&A, 657, A33
Alcalá, J. M., Biazzo, K., Covino, E., Frasca, A., & Bedin, L. R. 2011, A&A, 531, L12
Alexander, J. B. 1967, Obs, 87, 238
Amarsi, A. M., Lind, K., Asplund, M., Barklem, P. S., & Collet, R. 2016, MNRAS, 463, 1518
Andrievsky, S. M., Gorlova, N. I., Klochkova, V. G., Kovtyukh, V. V., & Panchuk, V. E. 1999, AN, 320, 35
Angelou, G. C., D'Orazi, V., Constantino, T. N., et al. 2015, MNRAS, 450, 2423
Anthony-Twarog, B. J., Deliyannis, C. P., Rich, E., & Twarog, B. A. 2013, ApJL, 767, L19
Asplund, M., Grevesse, N., Sauval, A. J., & Scott, P. 2009, ARA&A, 47, 481
Bailer-Jones, C. A. L., Rybizki, J., Fouesneau, M., Demleitner, M., & Andrae, R. 2021, AJ, 161, 147
Balachandran, S. C., Fekel, F. C., Henry, G. W., & Uitenbroek, H. 2000, ApJ, 542, 978
Barklem, P. S. 2018, A&A, 612, A90
Bernstein, R., Shectman, S. A., Gunnels, S. M., Mochnacki, S., & Athey, A. E. 2003, Proc. SPIE, 4841, 1694
Bharat Kumar, Y., Reddy, B. E., Muthumariappan, C., & Zhao, G. 2015, A&A, 577, A10
Binks, A. S., Jeffries, R. D., Sacco, G. G., et al. 2022, MNRAS, 513, 5727
Brown, J. A., Sneden, C., Lambert, D. L., & Dutchover, E., Jr. 1989, ApJS, 71, 293
Bruntt, H., Bedding, T. R., Quirion, P. O., et al. 2010, MNRAS, 405, 1907
Cai, B., Kong, X., Shi, J., et al. 2023, AJ, 165, 52
Cameron, A. G. W., & Fowler, W. A. 1971, ApJ, 164, 111
Canto Martins, B. L., Lèbre, A., de Laverny, P., et al. 2006, A&A, 451, 993
Canto Martins, B. L., Lèbre, A., Palacios, A., et al. 2011, A&A, 527, A94
Carlberg, J. K., Cunha, K., Smith, V. V., & Majewski, S. R. 2012, ApJ, 757, 109
Carlberg, J. K., Smith, V. V., Cunha, K., Majewski, S. R., & Rood, R. T. 2010, ApJL, 723, L103
Carlberg, J. K., Smith, V. V., Cunha, K., et al. 2015, ApJ, 802, 7
Carlsson, M. 1986, UppOR, 33, 2+39+117
Carlsson, M. 1992, in ASP Conf. Ser. 26, Cool Stars, Stellar Systems, and the Sun, ed. M. S. Giampapa & J. A. Bookbinder (San Francisco, CA: ASP), 499
Carney, B. W., Fry, A. M., & Gonzalez, G. 1998, AJ, 116, 2984
Casey, A. R. 2014, PhD thesis, Australian National Univ.
Casey, A. R., Ho, A. Y. Q., Ness, M., et al. 2019, ApJ, 880, 125
Casey, A. R., Ruchti, G., Masseron, T., et al. 2016, MNRAS, 461, 3336
Castellani, M., & Castellani, V. 1993, ApJ, 407, 649
Castelli, F., & Kurucz, R. L. 2004, A&A, 419, 725
Chanamé, J., Pinsonneault, M. H., Aguilera-Gómez, C., & Zinn, J. C. 2022, ApJ, 933, 58
Charbonneau, P., & Michaud, G. 1990, ApJ, 352, 681

Charbonnel, C., & Balachandran, S. C. 2000, A&A, 359, 563

Charbonnel, C., Brown, J. A., & Wallerstein, G. 1998, A&A, 332, 204

Charbonnel, C., Deliyannis, C. P., & Pinsonneault, M. H. 2000, arXiv:astro-ph/0006280

Charbonnel, C., & Lagarde, N. 2010, A&A, 522, A10

Charbonnel, C., Lagarde, N., Jasniewicz, G., et al. 2020, A&A, 633, A34

Charbonnel, C., & Talon, S. 2005, Sci, 309, 2189

Charbonnel, C., & Zahn, J. P. 2007, A&A, 467, L15

Cortés, C., Silva, J. R. P., Recio-Blanco, A., et al. 2009, ApJ, 704, 750

de la Reza, R., Drake, N. A., & da Silva, L. 1996, ApJL, 456, L115

de la Reza, R., Drake, N. A., da Silva, L., Torres, C. A. O., & Martin, E. L. 1997, ApJL, 482, L77

De Silva, G. M., Freeman, K. C., Bland-Hawthorn, J., et al. 2015, MNRAS, 449, 2604

Deal, M., & Martins, C. J. A. P. 2021, A&A, 653, A48

Deepak, & Lambert, D. L. 2021, MNRAS, 505, 642

Deepak, Lambert, D. L., & Reddy, B. E. 2020, MNRAS, 494, 1348

Deliyannis, C. P., Pinsonneault, M. H., & Charbonnel, C. 2000, in IAU Symp. 198, The Light Elements and their Evolution, ed. L. da Silva, R. de Medeiros, & M. Spite (Cambridge: Cambridge Univ. Press), 61

Deng, L.-C., Newberg, H. J., Liu, C., et al. 2012, RAA, 12, 735

Denissenkov, P., & Weiss, A. 2000, A&A, 358, L49

Denissenkov, P. A., & Herwig, F. 2004, ApJ, 612, 1081

D'Orazi, V., Gratton, R. G., Angelou, G. C., et al. 2015, ApJL, 801, L32

Drake, N. A., de la Reza, R., da Silva, L., & Lambert, D. L. 2002, AJ, 123, 2703

Dumont, T., Charbonnel, C., Palacios, A., & Borisov, S. 2021a, A&A, 654, A46

Dumont, T., Palacios, A., Charbonnel, C., et al. 2021b, A&A, 646, A48

Ezzeddine, R., Frebel, A., & Plez, B. 2017, ApJ, 847, 142

Ezzeddine, R., Plez, B., Merle, T., Gebran, M., & Thévenin, F. 2016, arXiv:1612.09302

Ezzeddine, R., Rasmussen, K., Frebel, A., et al. 2020, ApJ, 898, 150

Fekel, F. C., & Watson, L. C. 1998, AJ, 116, 2466

Fischer, D. A., & Valenti, J. 2005, ApJ, 622, 1102

Forestini, M., & Charbonnel, C. 1997, A&AS, 123, 241

Gao, Q., Shi, J.-R., Yan, H.-L., et al. 2019, ApJS, 245, 33

Gao, X., Lind, K., Amarsi, A. M., et al. 2020, MNRAS, 497, L30

Gonzalez, O. A., Zoccali, M., Monaco, L., et al. 2009, A&A, 508, 289

Gratton, R. G., & D'Antona, F. 1989, A&A, 215, 66

Gratton, R. G., Sneden, C., Carretta, E., & Bragaglia, A. 2000, A&A, 354, 169

Gruyters, P., Lind, K., Richard, O., et al. 2016, A&A, 589, A61

Gustafsson, B., Bell, R. A., Eriksson, K., & Nordlund, A. 1975, A&A, 42, 407

Gustafsson, B., Edvardsson, B., Eriksson, K., et al. 2008, A&A, 486, 951

Hanni, L. 1984, SvAL, 10, 51

Hansen, C. J., Primas, F., Hartman, H., et al. 2012, A&A, 545, A31

Hansen, T. T., Holmbeck, E. M., Beers, T. C., et al. 2018, ApJ, 858, 92

Harrington, P. Z., & Garaud, P. 2019, ApJL, 870, L5

Harutyunyan, G., Steffen, M., Mott, A., et al. 2018, A&A, 618, A16

Hekker, S., & Meléndez, J. 2007, A&A, 475, 1003

Hill, V., & Pasquini, L. 1999, A&A, 348, L21

Holmbeck, E. M., Hansen, T. T., Beers, T. C., et al. 2020, ApJS, 249, 30

Hunter, J. D. 2007, CSE, 9, 90

Iben, I., Jr. 1967, ApJ, 147, 624

Jasniewicz, G., Parthasarathy, M., de Laverny, P., & Thévenin, F. 1999, A&A, 342, 831

Ji, A. P., Frebel, A., Simon, J. D., & Chiti, A. 2016, ApJ, 830, 93

Jofré, E., Petrucci, R., García, L., & Gómez, M. 2015, A&A, 584, L3

Keeping, E. S. 1962, Introduction to Statistical Inference (Princeton, NJ: Van Nostrand)

Kelson, D. D. 2003, PASP, 115, 688

Kirby, E. N., Fu, X., Guhathakurta, P., & Deng, L. 2012, ApJL, 752, L16

Kirby, E. N., Guhathakurta, P., Zhang, A. J., et al. 2016, ApJ, 819, 135

Korn, A. J., Grundahl, F., Richard, O., et al. 2006, Natur, 442, 657

Kramida, A., Ralchenko, Y., Reader, J. & NIST ASD Team 2021, NIST Atomic Spectra Database (ver. 5.9) (Gaithersburg, MD: National Institute of Standards and Technology), https://physics.nist.gov/asd

Kumar, Y. B., & Reddy, B. E. 2020, JApA, 41, 49

Kumar, Y. B., Reddy, B. E., & Lambert, D. L. 2011, ApJL, 730, L12

Lagarde, N., Decressin, T., Charbonnel, C., et al. 2012, A&A, 543, A108

Lagarde, N., Reylé, C., Robin, A. C., et al. 2019, A&A, 621, A24

Lèbre, A., de Laverny, P., de Medeiros, J. R., Charbonnel, C., & da Silva, L. 1999, A&A, 345, 936

Lèbre, A., Palacios, A., Do Nascimento, J. D., Jr., et al. 2009, A&A, 504, 1011

Li, Y., & Ezzeddine, R., 2022 LOTUS: 1D Non-LTE Stellar Parameter Determination via Equivalent Width Method, Astrophysics Source Code Library, ascl:2207.017

Li, Y., & Ezzeddine, R. 2023, AJ, 165, 145

Lind, K., Asplund, M., Barklem, P. S., & Belyaev, A. K. 2011, A&A, 528, A103

Lind, K., Bergemann, M., & Asplund, M. 2012, MNRAS, 427, 50

Lind, K., Melendez, J., Asplund, M., Collet, R., & Magic, Z. 2013, A&A, 554, A96

Lind, K., Primas, F., Charbonnel, C., Grundahl, F., & Asplund, M. 2009, A&A, 503, 545

Lindegren, L., Bastian, U., Biermann, M., et al. 2021, A&A, 649, A4

Liu, Y. J., Tan, K. F., Wang, L., et al. 2014, ApJ, 785, 94

Luck, R. E. 1982, PASP, 94, 811

Lyubimkov, L. S. 2016, Ap, 59, 411

Lyubimkov, L. S., Lambert, D. L., Kaminsky, B. M., et al. 2012, MNRAS, 427, 11

Magrini, L., Lagarde, N., Charbonnel, C., et al. 2021a, A&A, 651, A84

Magrini, L., Smiljanic, R., Franciosini, E., et al. 2021b, A&A, 655, A23

Mallick, A., Reddy, B. E., & Muthumariappan, C. 2022, MNRAS, 511, 3741

Martell, S. L., & Shetrone, M. D. 2013, MNRAS, 430, 611

Martell, S. L., Simpson, J. D., Balasubramaniam, A. G., et al. 2021, MNRAS, 505, 5340

Mashonkina, L. I., Sitnova, T. N., & Pakhomov, Y. V. 2016, AstL, 42, 606

Masseron, T., Plez, B., Van Eck, S., et al. 2014, A&A, 571, A47

McWilliam, A., & Rich, R. M. 1994, ApJS, 91, 749

Monaco, L., Boffin, H. M. J., Bonifacio, P., et al. 2014, A&A, 564, L6

Monaco, L., Villanova, S., Moni Bidin, C., et al. 2011, A&A, 529, A90

Mori, K., Kusakabe, M., Balantekin, A. B., Kajino, T., & Famiano, M. A. 2021, MNRAS, 503, 2746

Mucciarelli, A., Monaco, L., Bonifacio, P., et al. 2022, A&A, 661, A153

Nordlander, T., Korn, A. J., Richard, O., & Lind, K. 2012, ApJ, 753, 48

Nordlander, T., & Lind, K. 2017, A&A, 607, A75

Osorio, Y., Barklem, P. S., Lind, K., et al. 2015, A&A, 579, A53

Palacios, A., Charbonnel, C., & Forestini, M. 2001, A&A, 375, L9

Placco, V. M., Frebel, A., Beers, T. C., & Stancliffe, R. J. 2014, ApJ, 797, 21

Placco, V. M., Sneden, C., Roederer, I. U., et al. 2021, RNAAS, 5, 92

Rebull, L. M., Carlberg, J. K., Gibbs, J. C., et al. 2015, AJ, 150, 123

Reimers, D. 1975, MSRSL, 8, 369

Reyniers, M., & Van Winckel, H. 2001, A&A, 365, 465

Richard, O., Michaud, G., & Richer, J. 2005, ApJ, 619, 538

Roederer, I. U., Hattori, K., & Valluri, M. 2018, AJ, 156, 179

Roederer, I. U., Preston, G. W., Thompson, I. B., et al. 2014, AJ, 147, 136

Roederer, I. U., Sakari, C. M., Placco, V. M., et al. 2018, ApJ, 865, 129

Ruchti, G. R., Fulbright, J. P., Wyse, R. F. G., et al. 2011, ApJ, 743, 107

Sackmann, I. J., & Boothroyd, A. I. 1992, ApJL, 392, L71

Sackmann, I. J., & Boothroyd, A. I. 1999, ApJ, 510, 217

Sakari, C. M., Placco, V. M., Farrell, E. M., et al. 2018, ApJ, 868, 110

Sayeed, M., Ness, M. K., Montet, B. T., et al. 2024, ApJ, 964, 42

Schlafly, E. F., & Finkbeiner, D. P. 2011, ApJ, 737, 103

Shappee, B., Prieto, J., Stanek, K. Z., et al. 2014, AAS Meeting, 223, 236.03

Siess, L., & Livio, M. 1999, MNRAS, 308, 1133

Silva Aguirre, V., Ruchti, G. R., Hekker, S., et al. 2014, ApJL, 784, L16

Singh, R., Reddy, B. E., & Kumar, Y. B. 2019, MNRAS, 482, 3822

Smiljanic, R., Franciosini, E., Bragaglia, A., et al. 2018, A&A, 617, A4

Smith, V. V., Shetrone, M. D., & Keane, M. J. 1999, ApJL, 516, L73

Sneden, C., Cowan, J. J., & Gallino, R. 2008, ARA&A, 46, 241

Sneden, C. A. 1973, PhD thesis, Univ. of Texas at Austin

Sobeck, J. S., Kraft, R. P., Sneden, C., et al. 2011, AJ, 141, 175

Soderblom, D. R., Fedele, S. B., Jones, B. F., Stauffer, J. R., & Prosser, C. F. 1993, AJ, 106, 1080

Strassmeier, K. G., Carroll, T. A., Weber, M., & Granzer, T. 2015, A&A, 574, A31

Susmitha, A., Mallick, A., & Reddy, B. E. 2024, ApJ, 966, 109

Takeda, Y., Zhao, G., Chen, Y.-Q., Qiu, H.-M., & Takada-Hidai, M. 2002, PASJ, 54, 275

Talon, S., & Charbonnel, C. 2010, in IAU Symp, 268, Light Elements in the Universe, ed. C. Charbonnel et al. (Cambridge: Cambridge Univ. Press), 365

Tayar, J., Ceillier, T., García-Hernández, D. A., et al. 2015, ApJ, 807, 82

Tody, D. 1986, Proc. SPIE, 627, 733

Tody, D. 1993, in ASP Conf. Ser. 52, IRAF in the Nineties, ed. R. J. Hanisch, R. J. V. Brissenden, & J. Barnes (San Francisco, CA: ASP), 173

Tognelli, E., Degl'Innocenti, S., Prada Moroni, P. G., et al. 2021, FrASS, 8, 22

Vassiliadis, E., & Wood, P. R. 1993, ApJ, 413, 641

Wallerstein, G., & Sneden, C. 1982, ApJ, 255, 577

Wang, E. X., Nordlander, T., Asplund, M., et al. 2021, MNRAS, 500, 2159
Wang, E. X., Nordlander, T., Asplund, M., et al. 2022, MNRAS, 509, 1521
Wenger, M., Ochsenbein, F., Egret, D., et al. 2000, A&AS, 143, 9
Wright, E. L., Eisenhardt, P. R. M., Mainzer, A. K., et al. 2010, AJ, 140, 1868
Yan, H.-L., Shi, J.-R., Zhou, Y.-T., et al. 2018, NatAs, 2, 790
Yan, H.-L., Zhou, Y.-T., Zhang, X., et al. 2020, NatAs, 5, 86
Yan, H.-L., Zhou, Y.-T., Zhang, X., et al. 2021, NatAs, 5, 86
Yong, D., Norris, J. E., Bessell, M. S., et al. 2013, ApJ, 762, 26
Zhang, X., & Jeffery, C. S. 2013, MNRAS, 430, 2113
Zhang, X., Jeffery, C. S., Li, Y., & Bi, S. 2020, ApJ, 889, 33
Zhou, Y. T., Shi, J. R., Yan, H. L., et al. 2018, A&A, 615, A74